

https://dspace.org/

A computational study of layered and superhard carbon-nitrogen material

Manyali, George Simiyu

2015-02-04
http://hdl.handle.net/10539/16867

Downloaded from a DSpace repository. https://dspace.org/

A computational study of layered and superhard carbon-nitrogen material

George Simiyu Manyali

August 2014

A thesis submitted to the Faculty of Science, University of the Witwatersrand, Johannesburg, in fulfilment of the requirements for the

degree of Doctor of Philosophy.



Declaration

I declare that this thesis is my own, unaided work. It is being submitted for the Degree of Doctor of Philosophy at the University of Witwatersrand, Johannesburg. It has not been submitted before for any degree or examination at any other University.

_____

(Signature of the candidate)

_____day of _____2014

Abstract

The process of the computational discovery of materials for future technologies is a combination of numerical techniques and general scientific intuition to select elements and combine in order to form novel types of materials. Modern *ab initio* methods based on density functional theory are capable of predicting with a high level of accuracy the most stable ground state atomic configurations of any given material. Once the ground state configurations are established, the electronic, optical and mechanical properties of the novel bulk nitrides may be determined.

Electronic properties of C_3N_4, CN_2, SiN_2, GeN_2, $C_2N_2(NH)$, $Si_2N_2(NH)$, $Ge_2N_2(NH)$ and $Sn_2N_2(NH)$ are analysed by computing the Kohn-Sham band structures. The optical properties are investigated by calculating the real and the imaginary parts of the frequency-dependent dielectric constant. The mechanical properties are determined by calculating elastic constants, Young's modulus, Poisson's ratio, Vickers hardness, shear and bulk moduli.

Publications

1. R. Warmbier, GS. Manyali and A. Quandt, **Surface plasmon polaritons in lossy uniaxial anisotropic materials**, Physical Review B 85 (8), 085442,9, (2012). Ref. [1]

2. GS. Manyali, R Warmbier, A Quandt and JE Lowther, **Ab initio study of elastic properties of super hard and graphitic structures of C_3N_4**, Computational Materials Science 69, 299-303, 3, (2013). Ref. [2]

3. GS. Manyali, R. Warmbier and A. Quandt, **Computational study of the structural, electronic and optical properties of $M_2N_2(NH)$: M = C, Si, Ge, Sn**, Computational Materials Science 79, 710714, (2013). Ref. [3]

4. A. Quandt, R. Warmbier and G. Manyali, **A multi-scale approach to computational photonics**, Electromagnetics in Advanced Applications (ICEAA), 2012 International Conference, 408-411, (2012). Ref. [4]

5. R. Warmbier, A. Quandt and G. Manyali, **Computational plasmonics for complex dielectric materials**, Electromagnetics in Advanced Applications (ICEAA), International Conference on, 470-473, (2012). Ref. [5]

6. A. Quandt, R Warmbier and GS Manyali, **Computational photonics from the bottom-up**, Transparent Optical Networks (ICTON), 14th International Conference, 1-4, (2012). Ref. [6]

7. GS. Manyali, R. Warmbier and A. Quandt, **Computational study of the structural, electronic and optical properties of dinitrides CN_2, SiN_2 and GeN_2** [7].

8. GS. Manyali, R. Warmbier and A. Quandt, **Optical properties of layered and cubic phases of C_3N_4** [in preparation].

9. GS. Manyali, R. Warmbier and A. Quandt, **Computational study of phase transition in carbon dinitrides**, [in preparation].

Dedication

To my late grandfather Philip Namonyo

Acknowledgement

Thanks to Professor Alexander Quandt for giving me an opportunity to work in his research group and for the best support I could wish for. Special thanks to Dr. Robert Warmbier for his reserved effort in reading my thesis and correcting errors. Thanks to Professors John E Lowther and Daniel Joubert for many discussions we had on material science and density functional theory. Other members of staff in school of Physics, especially Mr Lesias Kotane and Dr. Bheki Mathe are great mentors that am indebted to.

I also thank my colleagues Emily Aradi, Isaac Motochi, Ninon Gildas, Mahmud Abdulsalam, Moïse Dongho Nguimdo, Peter Egbele, Mohammed Suleiman, Mahlaga Molepo, Faris Mohammed among many fellow postgraduate students at the School of Physics for their stimulating discussions during coffee breaks.

I would like to thank Professor Sandro Scandolo and ASESMA executive board for the travel grants to attend CECAM School in Lausanne, Switzerland and the 7th International Conference of the Africa Materials Research Society in Addis Ababa, Ethiopia.

Finally, I would like to thank my four year old son Nicola Chetty for receiving my calls every day and singing to me those nice kids songs. Great appreciation to my wife, dad, mum, sisters and my brothers for their encouragement and prayers.

This thesis was fully funded by DST-NRF Centre of Excellence in Strong Materials, University of the Witwatersrand. This support is gratefully acknowledged. The Centre for High Performance Computing (CHPC), Cape Town (South Africa) is acknowledged for providing computational resources.

Contents

Declaration i

Abstract ii

publications iii

Dedication v

Acknowledgement v

Table of Contents viii

List of Figures xi

List of Tables xiii

1 Introduction 1

1.1 "Harder than diamond ?" 1

1.2 Objectives of the thesis 2

1.3 Thesis Scope and Outline 3

2 Computational discovery of materials 5

2.1 Structural phases of C_3N_4 6

2.2 Structural phases of carbon dinitride CN_2 6

2.3 Structural phases of Carbon Nitride Imide 9

3 Theoretical Framework **11**

3.1 Introduction . . . 11

3.2 The many-body system . . . 11

3.3 Density Functional Theory . . . 12

3.4 The Local Density Approximation . . . 15

3.5 Generalized gradient approximation . . . 16

3.6 Hybrid functionals and GW approximation . . . 16

3.7 Plane waves . . . 17

3.8 Dielectric constants . . . 20

3.9 Absorption coefficient . . . 21

3.10 Reflectivity . . . 22

3.11 Electron energy loss spectra . . . 22

3.12 Local field effects . . . 22

4 Computational results and discussion on C_3N_4 **23**

4.1 Computational details and structural properties . . . 23

4.2 Phase transition pressure . . . 24

4.3 Elastic properties of C_3N_4 . . . 27

4.4 Optical properties of C_3N_4 . . . 28

4.5 Derived optical properties . . . 33

4.6 Density of states and band gap . . . 34

4.7 Summary . . . 38

5 Computational results on carbon dinitrides (CN_2) **40**

5.1 Energy versus volume . . . 40
5.2 Phase Transition . . . 43
5.3 Summary . . . 47

6 Comparative studies of CN_2, SiN_2 and GeN_2 compounds 48

6.1 Equilibrium structural properties . . . 49
6.2 Mechanical and Dynamic Stability . . . 50
6.3 Derived elastic properties . . . 51
6.4 Electronic structure . . . 53
6.5 Optical Properties . . . 54
6.6 Summary . . . 56

7 Comparative studies of nitride imides 57

7.1 Structural and electronic properties . . . 57
7.2 Density of states and band gap . . . 59
7.3 Mechanical stability test . . . 60
7.4 Derived elastic properties . . . 61
7.5 Optical properties . . . 62
7.6 Summary . . . 64

8 Conclusions and future studies 66

8.1 Conclusions . . . 66
8.2 Future work . . . 68

References 80

List of Figures

2.1 The crystal structures for various phases of C_3N_4; (a) def. zinc-blende (b) cubic and (c) spinel, (d) hexagonal, (e) rhombohedral and (f) buckled geometry. The brown and grey spheres represent carbon atoms and nitrogen atoms respectively. 7

2.2 The crystal structures of (a) bct-CN_2, (b) I42m-CN_2, (c) pbam-CN_2, (d) p3m1-CN_2, (e) pbam-CN_2, (f) pa3-CN_2 and (g) pc-CN_2. The brown and grey spheres represent carbon atoms and nitrogen atoms respectively. 8

2.3 The orthorhombic crystal structural space group $Cmc2_1$. The blue, gray and red spheres represent M (where M =Si, C, Ge and Sn), N and H respectively 9

3.1 Convergence of Total Energy with Plane Wave Cut-off. 18

3.2 Convergence of Total Energy with k-point. 20

4.1 Total energy (eV/atom) versus volume/atom $V_0(Å^3)$ for various phases of C_3N_4. 25

4.2 The pressure-enthalpy curves for various phases of C_3N_4. 26

4.3 Real part of frequency-dependent dielectric function for diamond and several polymorphs of C_3N_4. For graphitic phases: Values without van der Waals correction has narrow black lines. The experimental (expt.) data for diamond was obtained from Ref. [8]. 30

4.4 Imaginary part of frequency-dependent dielectric function for diamond and several polymorphs of C_3N_4. For graphitic phases: Values without van der Waals correction has narrow black lines. The experimental (expt.) data for diamond was obtained from Ref. [8]. 31

4.5 Absorption spectrum of the frequency-dependent dielectric function for diamond and several polymorphs of C_3N_4. The experimental (expt.) data for diamond was obtained from Ref. [8]. 34

4.6 Reflectivity spectrum of frequency-dependent dielectric function for diamond and several polymorphs of C_3N_4. The experimental (expt.) data for diamond was obtained from Ref. [8]. 35

4.7 Electron energy loss spectra of the frequency-dependent dielectric function for diamond and several polymorphs of C_3N_4. The experimental (expt.) data for diamond was obtained from Ref. [8]. 36

4.8 Density of states for several polymorphs of C_3N_4 obtained using LDA. The Fermi level is set to the highest occupied band energy. 37

5.1 The total energy (eV/atom) versus volume/atom $V_0(Å^3)$ for various phases of CN_2. 41

5.2 The volume-pressure curves for various phases of CN_2. Volume decrease with increasing pressure and therefore pc-CN_2 phase is the zero-pressure stable structure. 42

5.3 Plot of enthalpy versus pressure obtained by fitting energy-volume data to EOS. The crossover between any two lines is interpreted as the transition pressure from one phase to another. 44

5.4 Phase transition pressure (a) P=13.24 GPa for pc-CN_2 $\rightarrow$ bct-CN_2 and (b) P=91.84 GPa for pc-CN_2 $\rightarrow$ pa3-CN_2. 44

5.5 Phase transition pressure (a) P=24.19 GPa for pc-CN_2 $\rightarrow$ cmc21-CN_2, (b) P=26.36 GPa for pc-CN_2 $\rightarrow$ I4m2-CN_2 and (c) P=7.20 GPa for p3m1-CN_2 $\rightarrow$ cmc21-CN_2. 45

5.6 Phase transition pressure (a) of P=8.81 GPa for p3m1-CN_2 $\rightarrow$ I4m2-CN_2, (b) P=28.81 GPa for p3m1-CN_2 $\rightarrow$ pbam-CN_2 and (c) P=64.45 GPa for p3m1-CN_2 $\rightarrow$ pa3-CN_2. 46

6.1 The base centered orthorhombic space group $Cmc2_1$ (No. 36) adopted by XN_2, where X= C, Si and Ge. The blue (large spheres) and red (small spheres) represent X and N respectively. 49

6.2 The real ε_1 and imaginary ε_2 parts of frequency-dependent dielectric function for CN_2, SiN_2 and GeN_2 calculated using PBEsol functional. 55

7.1 The curves showing energy per atom (eV) versus volume per atom(V) $Å^3$. The curves are obtained by fitting energy-volume data to third-order Birch-Murnaghan equations of states. 58

7.2 The averaged imaginary and real part of frequency depended dielectric function. The Infrared (IR), visible (V) and utraviolet (UV) spectral regions are indicated in the figure 64

List of Tables

4.1 Computational details for diamond and C_3N_4. Given are the number of atoms per unit cell, the size of the k-space mesh, the lattice parameter (a,c) in Å and the cohesive energy in eV/atom. For graphitic structures: Values without van der Waals corrections (Grimme's method) in brackets. 24

4.2 Computed elastic constants c_{ij} (GPa) for various C_3N_4 phases. For graphitic phases, elastic constants (in brackets) are obtained by inclusion of van der Waals interaction. 27

4.3 First principles results for elastic bulk modulus B(GPa), shear modulus G(GPa), G/B ratio, Young's modulus E(GPa), Poisson's ratio ν and predicted Vickers hardness H_v. The experimental values are in brackets. 28

4.4 Ion clamped static macroscopic dielectric constants ε_∞ and the ionic contribution ε^{ion} are calculated using DFPT method. ε_∞^{-lf} represents value without inclusion of local field effects while ε_∞^{+lf} represent those values with local field effects. The ionic contributions are given by ε^{ion}. For g-C_3N_4 the values of ε_∞ are reported as $\varepsilon_\perp/\varepsilon_\parallel$. The free electron plasma-frequency ω_p (eV) is shown as well. 32

4.5 Calculated energy band gap (eV) for several polymorphs of C_3N_4 calculated with different methods. Direct (d) and indirect(i) band gaps are indicated. 38

5.1 Calculated lattice constants a, b and c (Å), volume/atom V_0(Å^3), gravimetric density (gcm^{-3}), and bulk mudulus B_0 (GPa), derivatives of the bulk modulus B_0' and Cohesive energy E_{coh} (eV). 41

6.1 Calculated lattice constants a, b and c (Å), gravimetric density (gcm^{-3}), and volume V (Å^3). A comparison between experimental and other theoretical studies is also shown. 50

6.2 A comparison of independent elastic constants (GPa units) obtained using LDA, PBE and PBEsol. 51

6.3 Derived variables of elastic constants; bulk modulus B (GPa), shear G (GPa) and Young's modulus E (GPa), shear/bulk modulus ratio (G/B), Poisson's ratio ν and Vickers hardness (H_v) GPa. H_v is calculated from a semi-empirical model H_v=2(G^3/B^2)$^{0.585}$-3. 52

6.4 Calculated energy band gap (eV) for CN_2, SiN_2 and GeN_2 calculated with different methods. 54

6.5 Static macroscopic dielectric constants ε_∞ and the ionic contribution ε^{ion} are calculated using DFPT. ε_∞^{-lf} represents value without inclusion of local field effects while ε_∞^{+lf} represent those values with local field effects. The free electron plasma-frequency is denoted by ω_p (eV). Only results obtained using PBEsol are presented. 56

7.1 GGA-DFT calculated lattice constants (a, b and c) Å, gravimetric density (gcm^{-3}), volume per atom(V) Å^3, cohesive energy E_{coh}(eV), bulk modulus B_0 (GPa), and band gap E_g(eV). A comparison between experimental and other theoretical studies is also shown. 59

7.2 GGA-DFT calculated bondlengths in Å units. 60

7.3 Calculated independent elastic constants in GPa units obtained using GGA. . . . 61

7.4 First principles results for elastic bulk modulus B(GPa), shear modulus G(GPa), G/B, Young's modulus E(GPa), Poisson's ratio ν and predicted Vickers hardness H_v 62

7.5 GGA-DFT calculated dielectric constant along crystallographic axes $\mathbf{a}$, $\mathbf{b}$ and $\mathbf{c}$. . 63

1. Introduction

1.1 "Harder than diamond ?"

Hardness is an important macroscopic property of materials, which dictates their applications in various technological and industrial sectors. There are many ways of describing the hardness of a material. The simplest way is to correlate hardness to elastic and plastic deformations of a material. Hard materials are resistant to changes that may arise due to deformations.

Hardness of materials may be altered by variations in the pressure applied or by defects in the sample under consideration, and also by many other external factors such as temperature. As such, there are diverse hardness scales as described elsewhere [9]. Search for theoretical models to predict hardness has generated a lot of interest, leading to the development of semi-empirical theoretical models as elucidated by [10].

Hard materials exhibit diverse mechanical properties like elasticity, ductility, brittleness, toughness and durability. Furthermore, hard materials posses some distinct physical properties like electrical and thermal conductivity. Natural occurring hard materials are rare, and some of them have very specific applications, lacking wide industrial and technological applications.

Diamond is a naturally occurring carbon-based compound characterised by strong covalent bonds,high bulk and high shear moduli. Those characteristics of diamond makes it an attractive material for cutting, drilling, grinding and polishing applications [9, 11]. Structural and technological applications of diamond are quite different from those of other carbon allotropes like graphite, and two dimensional graphene [1, 5, 12–16].

Diamond is regarded to be hardest known material. This leads us to the question; Are there materials harder than diamond?

Search for materials harder than diamond remains a major scientific challenge. which is tackled by both experimentalist and theoreticians using different approaches, some of which are discussed in this thesis.

C_3N_4 has been postulated [17] to have mechanical properties rivalling that of diamond. This theoretical claim led to an explosion of scientific activities in early 1990s geared to deeper understanding of the novel C_3N_4 material. Several attempts were made to synthesize the material but without success. The failure may partly be attributed to a lack of required apparatus that would go beyond the existing diamond anvil cell in order to realize high pressure and high temperature conditions [18,19]. However, from a theoretical perspective, it is clear that the cubic C_3N_4 should have a larger bulk modulus than diamond. On the contrary, the shear modulus of diamond is far greater than that of cubic C_3N_4. The Vickers hardness investigated using various semi-empirical models predict a softer cubic C_3N_4 compared to diamond. Correlation between hardness and either shear and bulk moduli have revealed that their exist a strong coupling between hardness and shear moduli [9, 18].

Search for candidate superhard materials beyond C_3N_4 has not established novel candidate materials harder than diamond. Extensive research on the properties of nitrides like cubic boron nitride, zirconium nitride, titanium nitride and silicon nitride [20–22] indicate that these materials have inferior hardness properties compared to diamond.

Therefore "Harder than diamond?" remains an open question, which this thesis seeks to potentially answer by proposing novel candidate superhard materials, and by calculating wide range of their basic materials properties.

1.2 Objectives of the thesis

1. To provide an overview of elastic properties of the hypothetical superhard C_3N_4.
2. To perform comparative studies of the optical properties of the cubic and layered phases of C_3N_4.
3. To carry out a thorough investigation of the phase transformations in carbon dinitride (CN_2).
4. To perform a comparative study of the electronic material properties of CN_2, SiN_2 and GeN_2

5. To perform a comparative study of the electronic material properties of $C_2N_2(NH)$, $Si_2N_2(NH)$, $Ge_2N_2(NH)$ and $Sn_2N_2(NH)$.

1.3 Thesis Scope and Outline

This thesis is a continuation of my Master of Science work [9] which focused mainly on the elastic properties of C_3N_4. The current work provides an overview of the elastic properties (shear and bulk moduli), and how they correlate with Vickers hardness. Also, the optical properties of C_3N_4 are discussed in detail, comparing the frequency dependent dielectric function for diamond-like and graphite-like C_3N_4 structures. The knowledge gained from the study of the properties of C_3N_4, is used to predict new low compressible materials CN_2 and $C_2N_2(NH)$, whose properties are also discussed in this thesis.

The thesis is organised as follows;

Chapter 1 provides a brief introduction on the properties of diamond and superhard nitrides. The significance of hardness and the need for materials with hardness surpassing that of diamond are also briefly discussed in this chapter.

Chapter 2 gives an account of several crystal structures adopted by the compounds studied in this work.

Chapter 3 gives a background information on density functional theory (DFT), exchange-correlation functionals and the most crucial convergence tests for any DFT calculations. The formalism for calculating frequency dependent dielectric function is also elaborated in this chapter.

Chapter 4 discusses crucial results concerning the Vickers hardness, dielectric function and band gaps of various polymorphs of C_3N_4.

Chapter 5 illustrates the process of searching for novel stable and low compressible materials. Phase diagrams of CN_2 are discussed. One stable phase is picked among many alternative phases and calculations of elastic and optical properties are performed and discussed in Chapter 6.

Chapter 6 also provides insight into general effects of DFT exchange-correlation functionals on

some of the material properties of isostructural compounds CN_2, SiN_2 and GeN_2.

Chapter 7 discusses the electronic structure properties of imides formed by incorporating hydrogen in various nitrides.

Some general remarks, a short summary and an outlook are given in chapter 8.

2. Computational discovery of materials

The process of computational discovery of materials for future technologies is a combination of numerical techniques and general scientific intuition to select elements to combine and form novel types of materials. The practical application of novel computationally discovered materials is rarely ever realised immediately and may even stretch to decades before they are assimilated in a new technology. This may be attributed to challenges in carrying out experiments, but also to the pros and cons of the properties of newly discovered materials against the existing ones in the market.

The computational discovery of materials is therefore not only inspired by the search for the substitute of existing materials, but also to create data repositories, where scientist and engineers can retrieve appropriate materials whenever the need for specified materials properties may arise. The computational techniques for discovering new materials are evolving rapidly as has been witnessed in the past decade. This tremendous progress is aided by the development of supercomputers with powerful abilities to explore several thousands of candidate materials and crystal structures within a short span of time. Density functional theory (DFT) [23, 24] is used to compute the ground state properties of materials. The level of accuracy of predicted materials properties is usually very good with respect to experimental data. However, DFT does have its shortcomings. The most prominent one is the band-gap problem which affects calculation of optical properties. DFT always underestimates the band gap due to an intrinsic problem with electron-hole interactions. Nevertheless, the band structure above the band gap is often qualitatively correct.

The starting point of any DFT calculation is the atomic structure of a solid. The crystallographic databases, such as International Crystallographic Structural Database (ICSD) [25, 26] have been a resourceful 'basket' with thousands of prototype crystal structure for different elements. There is a growing trend of new multidimensional databases such as the Materials Project [27] and the materials structure library based on the AFLOW software [28]. The AFLOW software is one example of high-throughput modelling developed to explore potential alloy materials by examining different crystal structures and comparing their minimum energies, so as to select the energetically favourable and thus most stable structures.

2.1 Structural phases of C_3N_4

C_3N_4 has been predicted to exist in different phases, attractive for a variety of technological applications [17, 29–39]. The following C_3N_4 structural phases and their symmetry representations are investigated: Defect zinc-blende belong to a space group $P\bar{4}2/m$ which can be easily constructed from diamond structure without one atom. The cubic structure with space group $I\bar{4}3d$ is analogous to Zn_2SiO_4 structure, where Zn and Si atoms are substituted for C atoms, while O atoms are substituted for N atoms. Furthermore, the Fe and O atoms in Fe_3O_4 structure are substituted for C and N atoms to form the spinel structure of C_3N_4 with space group $Fd\bar{3}m$. These three C_3N_4 compounds have a lot of similarities with diamond, henceforth referred to as diamond-like C_3N_4. The layered structures resemble somehow graphite, comprise of the hexagonal structure with space group $P\bar{6}m2$ and the rhombohedral/trigonal structure identified by the space group $R3m$. These structures are characterized by honeycomb patterns based on the triazine structure [2, 18, 40–42]. For the sake of comparison an A-B stacked melon structure with clustered heptazine honeycombs was also considered. Note that the R_{3m} space group has a rhombohedral and hexagonal representation, where the smaller rhombohedral cell is not aligned with the optical axis, therefore the hexagonal supercell was used for the calculations. Density functional theory (DFT) calculations have also shown that the idealised planar graphitic structures are not mechanically stable [2]. Relaxing the unit cells, one finds numerous minima with small out-of-plane distortions with very similar energies. This suggests, that real graphitic C_3N_4 should show a disordered structure. The mechanically stable buckled geometry based on the rhombohedral C_3N_4 [2] is considered later on to cross-check the influence of those small distortions on the optical properties.

2.2 Structural phases of carbon dinitride CN_2

Recently, Weihrich et al. [43, 44] proposed a pyrite structure of CN_2 (space group $Pa\bar{3}$) isoelectronic to SiP_2. The authors argue that their choice for the hypothetical pyrite structure was guided by the conserved three-dimensional network of CN bonds, as well as and the simplicity of

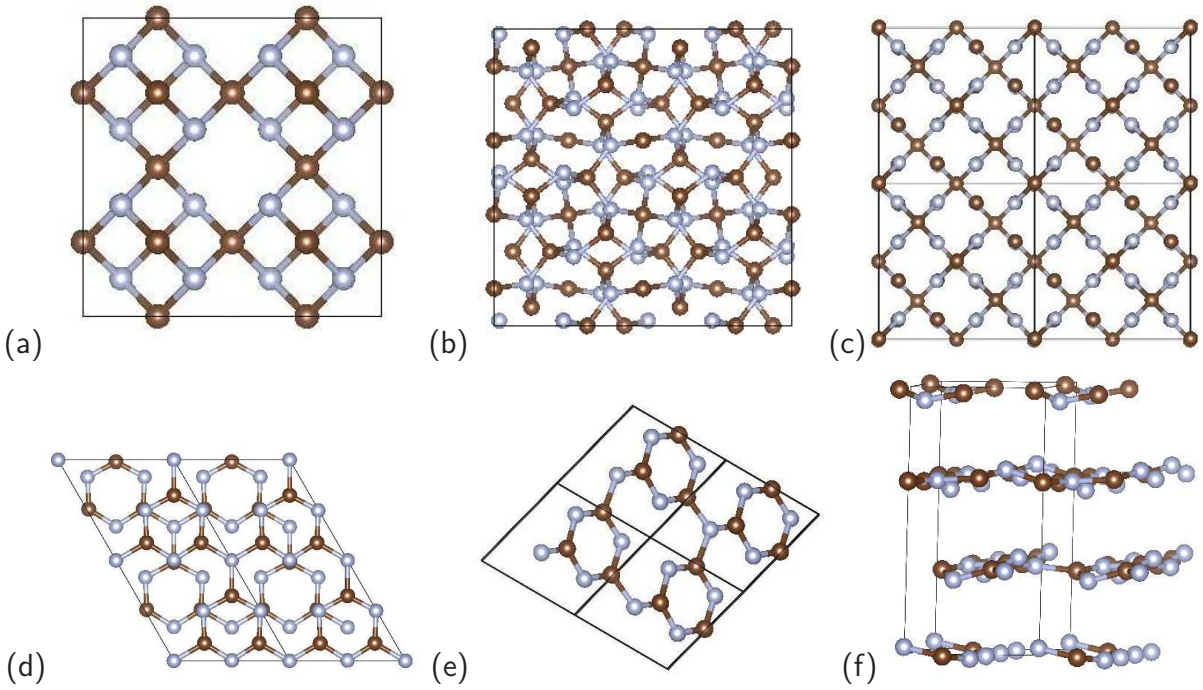


Figure 2.1 The crystal structures for various phases of C_3N_4; (a) def. zinc-blende (b) cubic and (c) spinel, (d) hexagonal, (e) rhombohedral and (f) buckled geometry. The brown and grey spheres represent carbon atoms and nitrogen atoms respectively.

the structure. Five polytypic structures for CN_2 with space groups $P\bar{4}2_1m$, $I\bar{4}2d$, $I\bar{4}m2$, $P\bar{3}m1$ and $Cmc2_1$ were explored in the theoretical work of Quan et al. [45]. The two research groups found that carbon nitride of the stoichiometry CN_2, is a low compressible material exhibiting elastic properties that are identical to some phases of C_3N_4. In the present work, prototype crystal structures are obtained from the ICDS database. The phase transformation properties of CN_2, are studied in a thermodynamics framework based on Gibbs free energies. The seven crystal structures described by their space groups are as follows: space group $Cmc2_1$ denoted as cmc21-CN_2, space group $P\bar{3}m1$ denoted as p3m1-CN_2 and space group $P\bar{4}2_1m$ denoted as pc-CN_2. Furthermore, the space group $I\bar{4}2d$ denoted as bct-CN_2, space group $I\bar{4}2m1$ denoted as I42m-CN_2, space group $Pa\bar{3}$ denoted as pa3-CN_2 and space group Pbam denoted as pbam-CN_2 were also considered. As noted earlier, the process of computational discovery of material requires prior knowledge of the basic principles of chemical and structural formations of compounds. For example, the group IV elements in the period table are Carbon(C), Silicon(Si), Germanium(Ge)

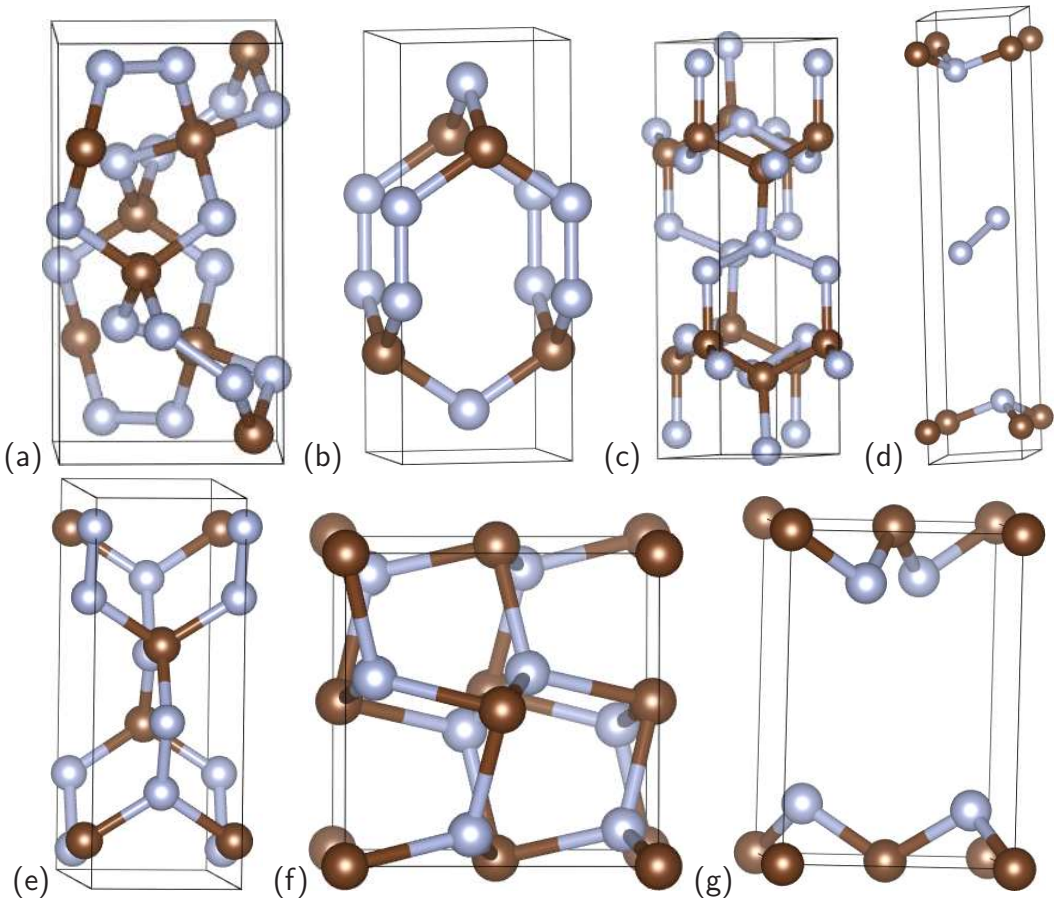


Figure 2.2 The crystal structures of (a) bct-CN_2, (b) I42m-CN_2, (c) pbam-CN_2, (d) p3m1-CN_2, (e) pbam-CN_2, (f) pa3-CN_2 and (g) pc-CN_2. The brown and grey spheres represent carbon atoms and nitrogen atoms respectively.

and Tin(Sn). They have similar chemical properties. If one knows which structure C adopts, then one may think of replacing C with the rest of the elements in that group. This method has successfully been used to predict both silicene and germanene [46] from graphene [14]. This strategy has also been applied to reveal interesting structural, electronic and optical properties of SiN_2 and GeN_2, which are discussed in detail later on.

2.3 Structural phases of Carbon Nitride Imide

High pressure and high temperature technique have been widely used for the synthesis of the nitrogen-based compounds such as the crystallized binary Si_3N_4. There have also been reports on the synthesis of the ternary nitrides knowns as carbon nitride imide ($C_2N_2(NH)$). First successful synthesis of $C_2N_2(NH)$ was performed by Hovarth-Bordon et al. [47]. Their measurements revealed that $C_2N_2(NH)$ crystallises into a base-centred orthorhombic (bco) structure, a defect-wurtzite structure with space group $Cmc2_1$ similar to the structure adopted by Si_2N_2O (see Figure 2.3).

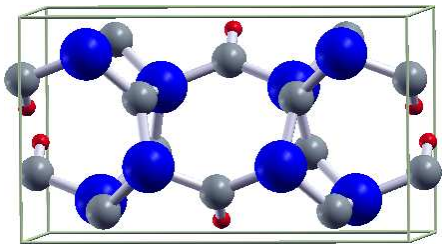


Figure 2.3 The orthorhombic crystal structural space group $Cmc2_1$. The blue, gray and red spheres represent M (where M =Si, C, Ge and Sn), N and H respectively

The physical properties of $C_2N_2(NH)$ such as density and bulk modulus were observed to mimic that of dense C_3N_4. Immediately after the work of Hovarth-Bordon et al., other experimentalist [48] independently confirmed that $C_2N_2(NH)$ crystallises in a bco structure. These experimental findings have been backed-up by theoretical calculations and further experimental measurements of physical properties [3, 49–52]. The continuous process of computational exploration of new materials and data mining led to discovery of $C_2N_2(CH_2)$ form of carbon nitride [53]. Both $C_2N_2(CH_2)$ and $C_2N_2(NH)$ crystallize in the bco structure, and they are mechanically stable. The two compounds have been predicted to have Vickers hardness close to 40 GPa [52], and hence qualify as superhard materials.

The search for superhard materials via theoretical modelling has led to discovery of new nitride imides, which may be obtained from $C_2N_2(NH)$ by replacing C with Ge and Sn [3]. This technique of computational discovery of materials is fundamentally quite successful since diverse elements in the periodic table show similar characteristics such as being isoelectronic or isostructural. A

comparative study of the electronic structure properties of $C_2N_2(NH)$, $Si_2N_2(NH)$, $Ge_2N_2(NH)$ and $Sn_2N_2(NH)$ are part of this thesis.

3. Theoretical Framework

3.1 Introduction

There is no doubt that quantum theory has ability to provide fundamental understanding and sufficient information on the physics, chemistry and biology of materials by simply studying their ions and electrons. This implies that ions and electrons are important parameters in any quantum mechanical calculations. Using quantum theory, one is able to distinguish between metals and insulators, or one is able to characterise materials based on their optical, magnetic and elastic properties.

3.2 The many-body system

A complete description of the quantum mechanical behavior of atoms requires detailed consideration of interactions between electrons and nuclei [54].

Let $\hat{H}$ denote the Hamiltonian of a many electron system. The states of well-defined energy are the eigenstates of $\hat{H}$:

$$\hat{H}\Psi_k(r_1\sigma_1\ldots,r_N\sigma_N) = E_k\Psi_k(r_1\sigma_1\ldots,r_N\sigma_N). \tag{3.2.1}$$

where k, is a complete set of many-electron quantum numbers, Ψ is the electron wave function while E is the total energy of the system. The particles with half integer spins, such as electrons, are described by an antisymmetric wave functions

$$\Psi(r_1\sigma_1\ldots,r_i\sigma_i,\ldots,r_j\sigma_j,\ldots,r_N\sigma_N) = -\Psi(r_1\sigma_1\ldots,r_j\sigma_j,\ldots,r_i\sigma_i,\ldots,r_N\sigma_N), \tag{3.2.2}$$

and they obey the Pauli exclusion principle. Such particles are termed fermions. The Pauli exclusion principle states that no two electrons can have the same set of quantum numbers, and electrons with the same spin cannot occupy the same state simultaneously. Those particles whose wave functions are symmetric under particle interchange and have integral or zero intrinsic spin are called bosons.

Note that there are $N!$ distinct permutations of the labels $1, 2, ..., N$, which by Eq. (3.2.2) all have the same $|\Psi|^2$. Hence, the probability to find any electron with spin σ_1 in volume element d^3r_1, is

$$N!|\Psi_k(r_1\sigma_1 \ldots, r_N\sigma_N)|^2 d^3r_1 ... d^3r_N. \tag{3.2.3}$$

A proper Hamiltonian operator $\hat{H}$ taking into account all the interactions between electrons and nuclei is given as,

$$\hat{H} = -\frac{\hbar^2}{2m_e}\sum_i \nabla_i^2 + \sum_{i,I}\frac{Z_I e^2}{\mid r_i - R_I \mid} + \frac{1}{2}\sum_{i \gtrless j}\frac{e^2}{\mid r_i - r_j \mid} - \sum_I \frac{\hbar^2}{2M_I}\nabla_I^2 + \frac{1}{2}\sum_{I \gtrless J}\frac{Z_I Z_J e^2}{\mid R_I - R_J \mid}, \tag{3.2.4}$$

where electron mass m_e and charge e are represented by lower case subscripts, while the nuclei with mass M_I and core charge Z_I are denoted by upper case subscripts [55]. The terms in the equation 3.2.4 above are the electronic kinetic energy operator $\hat{T}_e = -\frac{\hbar^2}{2m_e}\sum_i \nabla_i^2$, the nuclei potential acting on the electrons $\hat{V}_{en} = \sum_{i,I}\frac{Z_I e^2}{|r_i - R_I|}$, the repulsion from the electron-electron interactions is denoted by $\hat{V}_{ee} = \frac{1}{2}\sum_{i \gtrless j}\frac{e^2}{|r_i - r_j|}$, the nuclei kinetic operator $\hat{T}_n = -\sum_I \frac{\hbar^2}{2M_I}\nabla_I^2$ and the repulsion due to nuclei-nuclei interactions operator $\hat{V}_{nn} = \frac{1}{2}\sum_{I \gtrless J}\frac{Z_I Z_J e^2}{|R_I - R_J|}$. The terms in the equation 3.2.4 may be written in the simplest form as,

$$\hat{H} = \hat{T}_e + \hat{V_{en}} + \hat{V_{ee}} + \hat{T}_n + \hat{V_{nn}}. \tag{3.2.5}$$

3.3 Density Functional Theory

The concept of density functional theory (DFT) was conceived in 1960s by Hohenberg, Kohn and Sham [23, 24] but the concept only became popular in the 1980s. Thereafter, DFT has become a standard tool for predicting the electronic properties of materials. In DFT, the electronic density distribution $n(r)$ is considered to be the basic property of a many-electron wave function Ψ [56].

Currently, there are numerous ab initio codes in which DFT has been implemented. One of those codes is the Vienna Ab-Initio Simulation Package (VASP). VASP code uses the plane-wave basis in performing *ab initio* quantum mechanical molecular dynamics calculations. The projector

augmented wave pseudopotentials, which are more accurate than the ultra-soft pseudopotentials are implemented in VASP [57–60].

A brief description of density functional theory ingredients are discussed below.

3.3.1 The Hohenberg-Kohn Theorem. The Hohenberg-Kohn theorem is applicable to any system of interacting electrons subjected to an external potential. The theory states that if a system with N interacting electrons is under the influence of an external potential V_{ext}, then a unique ground-state electron density $n_0(\mathbf{r})$ minimizes the corresponding energy functional,

$$E[n] = F[n] + \int n(\mathbf{r}) V_{ext}(\mathbf{r}) \mathrm{d}\mathbf{r}. \tag{3.3.1}$$

where F is a universal functional of n. Hence the total ground-state electronic energy E_0, is simply the minimum of the functional E. To prove the Hohenberg-Kohn theorem, Levy [61] defined a general N-electron functional F as

$$F[n(r)] = \min_{|\Psi \to n(r)|} \left\langle \Psi | \hat{F} | \Psi \right\rangle, \tag{3.3.2}$$

where the expectation value is determined by searching over all N-electron wave functions, Ψ, which reduce to a given density $n(\mathbf{r})$. One then selects the wave function Ψ which effectively minimizes the expectation value of $\hat{F}$. Note that $\hat{F}$ is

$$\hat{F} = \sum_i -\frac{1}{2} \bigtriangledown_i^2 + \frac{1}{2} \sum_{i \neq j} \frac{1}{|\mathbf{r_i} - \mathbf{r_j}|}. \tag{3.3.3}$$

Now consider an N-electron ground state wave function Ψ_0 which yields a density n_0. Then the ground state energy is

$$E_0 = \left\langle \Psi_0 | \hat{F} + \hat{V}_{ext} | \Psi_0 \right\rangle \tag{3.3.4}$$

From equation (3.3.2) we know that

$$F[n_0] = \min_{\Psi \to n_0} \left\langle \Psi | \hat{F} | \Psi \right\rangle = \left\langle \Psi^0_{min} | \hat{F} | \Psi^0_{min} \right\rangle, \tag{3.3.5}$$

and from the minimum principle

$$F\left[n_0\right] + \int \hat{V}_{ext}\, n_0(r) d^3r = \left\langle \Psi^0_{min} | \hat{F} + \hat{V}_{ext} | \Psi^0_{min} \right\rangle \geqslant E_0 \tag{3.3.6}$$

However, since

$$F\left[n_0\right] = \left\langle \Psi^0_{min} | \hat{F} | \Psi^0_{min} \right\rangle \leq \left\langle \Psi_0 | \hat{F} | \Psi_0 \right\rangle \tag{3.3.7}$$

we also have

$$F\left[n_0\right] + \int \hat{V}_{ext}\, n_0(r) d^3r = \left\langle \Psi^0_{min} | \hat{F} + \hat{V}_{ext} | \Psi^0_{min} \right\rangle \leq E_0 \tag{3.3.8}$$

since Ψ^0_{min} and Ψ_0 yield the same density n_0. From equations (3.3.6) and (3.3.8) it follows that

$$E\left[n_0\right] = F\left[n_0\right] + \int \hat{V}_{ext}\, n_0(r) d^3r = E_0 \tag{3.3.9}$$

thereby completing the proof.

3.3.2 The Kohn-Sham Equations. In the Hohenberg-Kohn theorems [23], the exact form of the universal functional F is unknown. In order to turn this into a potential scheme Kohn and Sham [24], assumed that the ground-state density $n_0(\mathbf{r})$ is the density of non-interacting reference system. The functional $F\left[n(\mathbf{r})\right]$ is separated into four parts and hence E becomes,

$$E\left[n(\mathbf{r})\right] = T_s\left[n(\mathbf{r})\right] + \frac{1}{2}\int\int \frac{n(\mathbf{r}) n(\mathbf{r}')}{|\mathbf{r} - \mathbf{r}'|} d\mathbf{r} d\mathbf{r}' + E_{XC}[n(\mathbf{r})] + \int n(\mathbf{r}) V_{ext}(\mathbf{r}) d\mathbf{r}, \tag{3.3.10}$$

where $T_s\left[n(\mathbf{r})\right]$ is the kinetic energy of a non-interacting electron gas with density $n(\mathbf{r})$, i.e.

$$T_s\left[n(\mathbf{r})\right] = -\frac{1}{2}\sum_i^N \int \Psi_i^*(\mathbf{r}) \nabla^2 \Psi_i(\mathbf{r}) d\mathbf{r}. \tag{3.3.11}$$

Equation (3.3.10) also defines a general exchange-correlation functional $E_{XC}\left[n\right]$. Imposing a normalization constraint on the electron density, $\int n(\mathbf{r}) d\mathbf{r} = N$, one obtains the following variational principle

$$\begin{aligned} \frac{\delta}{\delta n(\mathbf{r})}\left[E\left[n(\mathbf{r})\right] - \mu \int n(\mathbf{r}) d\mathbf{r}\right] = 0 \\ \Rightarrow \frac{\delta E\left[n(\mathbf{r})\right]}{\delta n(\mathbf{r})} = \mu. \end{aligned} \tag{3.3.12}$$

μ is the chemical potential. Equation 3.3.12 may now be re-written in terms of an effective potential, $V_{eff}(\mathbf{r})$, and that

$$\frac{\delta T_s\left[n(\mathbf{r})\right]}{\delta n(\mathbf{r})} + V_{eff}(\mathbf{r}) = \mu, \tag{3.3.13}$$

where

$$V_{eff}(\mathbf{r}) = V_{ext}(\mathbf{r}) + \int \frac{\mathbf{n}(\mathbf{r})}{|\mathbf{r}-\mathbf{r}|}\mathrm{d}\mathbf{r}' + V_{XC}(\mathbf{r}) \tag{3.3.14}$$

with

$$V_{XC}(\mathbf{r}) = \frac{\delta E_{XC}[n(\mathbf{r})]}{\delta n(\mathbf{r})}, \tag{3.3.15}$$

It is important to note that non-interacting electrons moving in an external potential $V_{eff}(r)$ are described by a ground state density

$$n_0(\mathbf{r}) = \sum_{i=1}^{N} |\Psi_i(\mathbf{r})|^2, \tag{3.3.16}$$

Variation of the $E[n(\mathbf{r})]$ with respect to $\Psi_i^*(k)$ leads to following one electron Schrödinger equation

$$\left(\frac{1}{2}\nabla_i^2 + V_{eff}(r) - E_i\right)\Psi_i(r) = 0 \tag{3.3.17}$$

and this set of equations should be solved self-consistently as

$$V_{eff}(r) = V_{eff}(n_0(r)). \tag{3.3.18}$$

In summary, if one considers a non-interacting reference system, then the equations (3.3.13) and (3.3.14) would provide a theoretically exact method for finding the ground state energy E_0 of an interacting system, provided that E_{XC} is known. Search for the exact form of E_{XC} is an ongoing research. Some proposals have been made, tested on a number of materials but the results have always been a mixture of success and failure. Some of this E_{XC} functionals are discussed below.

3.4 The Local Density Approximation

The local density approximation (LDA) [62] is one of the most significant functionals that was proposed by Hohenberg and Kohn in early 1960s. The idea was to locally approximate the exchange-correlation energy $E_{XC}[n(\mathbf{r})]$ of an interacting electron system by the exchange-correlation energy of homogeneous electron gas of density $n(\mathbf{r})$, i.e.,

$$E_{XC}^{LDA}[n(\mathbf{r})] = \int \mathbf{E}_{XC}(n(\mathbf{r}))n(\mathbf{r})d\mathbf{r}. \tag{3.4.1}$$

LDA is the oldest exchange-correlation function, and the formalism has some weaknesses. It fails to predict correctly the magnetic properties of bulk material and it underestimate the band gap up to 50% or more [63–67].

3.5 Generalized gradient approximation

Development of GGA exchange-correlation functionals was the result of an assumption by Hohenberg and Kohn that LDA would fail in real systems. They proposed a new scheme called gradient expansion approximation (GEA). The work of Hohenberg and Kohn was developed further by Perdew and co-workers [68–70], proposing general functionals of the kind

$$E_{XC}^{GGA}[n] = \int d^3r f(n, \nabla n) \tag{3.5.1}$$

where $E_{XC}^{GGA}[n]$ define the exchange correlation energy. The GGA method gives better results for predicting molecular geometries and ground-state energies, but it is computationally more expensive than LDA [71]. GGA is also reliable for predicting magnetic properties of 3d transition metals [72, 73]. Despite all that success, GGA has its limitations. It fails to predict correctly the lattice parameters of graphite and does not accurately treat hydrogens bond [74]. More advanced and probably more accurate than the GGA functionals are the new meta-GGA functionals like the ones parametrized by Tao-Perdew-Staroverov-Scuseria (TPSS) [75].

3.6 Hybrid functionals and GW approximation

Semiconducting materials are important technological materials with very wide applications. Therefore, it is important to have *ab initio* methods that accurately describes their properties. Both LDA and GGA, usually underestimate their band gaps, while the Hatree-Fock methods overestimates the band gap. Suitable functionals that predict accurate band gaps should be obtained by suitable admixture of the local or semilocal DFT exchange energy functionals and the non-local Hartree-Fock exchange energies. Hybrid functionals like HSE06 have been proposed to address the band gap problem [76, 77]. These methods are often reliable in predicting band

gaps, but they are also computationally expensive. Another method that is also computationally expensive but produce accurate results of the band gaps is the GW approximation [78]. All these methods are limited to smaller systems, especially when computational resources are limited. The modified Becke-Johnson (MBJ) potentials [79, 80] have of late attracted much attention as the simplest method for calculating accurate band gaps. This method requires minimal computational resources and its accuracy is almost of the same level as HSE06 and GW.

3.7 Plane waves

Computational modelling of solids requires a proper definition of the unit cell defined by the unit vectors $\vec{a_1}$, $\vec{a_2}$ and $\vec{a_3}$. For crystalline solids, atoms are usually arranged in a regular repeating pattern. Furthermore, if the nuclei are arranged in a periodically repeating pattern, then their lattice potential U(r) acting on the electrons must also be periodic. As such the single electron Schrödinger equation under periodic potential U(r) is writen as [81, 82];

$$\left(-\frac{1}{2}\nabla^2 + U(r)\right)\Psi = \varepsilon\Psi \tag{3.7.1}$$

The Bloch theorem states that the one-electron wavefunctions obey the equation

$$\Psi_k(r) = \exp^{ik.r}\,\mu_k(r), \tag{3.7.2}$$

where $\mu_k(r)$ has the periodicity of the lattice. This allows the plane wave expansion of the electron wavefunctions ,

$$\Psi_{i,k}(r) = \sum_G c_{i,k+G}\mathrm{e}^{i(k+G).r} \tag{3.7.3}$$

where the G are the reciprocal lattice vectors. The Kohn-Sham equations in $\mathbf{k}$ space then reduce to the following matrix eigenvalue equation

$$\sum_{G'}\{\frac{1}{2}|k+G|^2\delta_{GG'} + V_{ext}(G-G') + V_H(G-G') + V_{xc}(G-G')\}c_{i,k+G} = \epsilon_i c_{i,k+G}. \tag{3.7.4}$$

where V_{ext} is the static total electron-ion potential, V_H is the Hartree potential of the electrons, i and ϵ are the Kohn-Sham eigenvalue, V_{xc} is the exchange-correlation potential and $c_{i,k+G}$ is the

coefficient of plane-wave basis state. In practice, not all wave vectors are needed, hence a cut-off energy defined as

$$E_{cut} = \frac{1}{2}|k + G_{max}|^2, \tag{3.7.5}$$

is used. E_{cut} is the kinetic energy cut-off.

3.7.1 Energy Cut-Off. The cut-off energy for plane wave basis is a significant parameter in DFT calculations. The convergence of the cut-off energy with respect to the total energy is evaluated at a fixed k-point-mesh and experimental lattice parameter or lattice parameter obtained from the existing crystallographic databases. An example of energy cut-off convergence (for the defect zinc-blende structure of the C_3N_4) is shown in the Figure 3.1. As one can see a cut-off energy

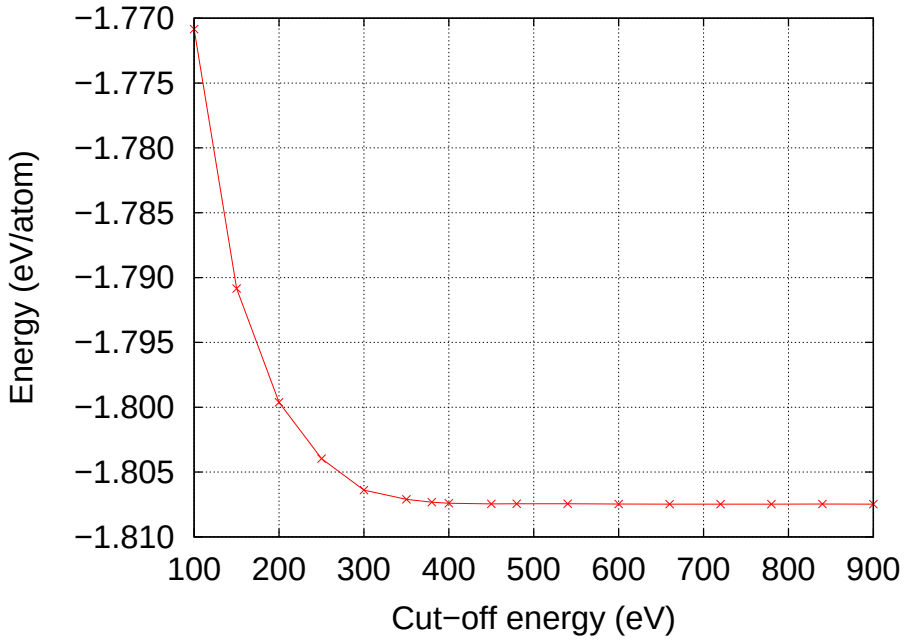


Figure 3.1 Convergence of Total Energy with Plane Wave Cut-off.

below 400 eV was insufficient. Therefore, one must choose values above the default cut-off energy(400 eV) in order to obtain accurate results. Very high cut-off energies are undesirable since they only increases the computational cost without really improving the accuracy of the results. The pseudopotentials that come along with VASP usually have a default cut-off energy. In the case of of carbon nitride materials with two species (i.e carbon and nitrogen), the maximum cut-off energy in each case is 400 eV. Hence the 400 eV is indeed the minimum value for a cut-off

energy that will give reasonable results.

3.7.2 K-points. The first Brillouin zone is defined as the Wigner-Seitz cell of the reciprocal lattice described by the planes that are perpendicular bisectors between the lattice points and the origin of the reciprocal lattice [55]. The commonly used technique in sampling the first Brillouin zone is the uniformly spaced Monkhorst-Pack k-point grid [83]. There is another sampling scheme proposed by Chadi and Cohen [84] which has received less attention as compared to the Monkhorst-Pack k-point grid. The Monkhorst-Pack grids are denoted as $n1 \times n2 \times n3$ grids, which results in a total number of k-points presented as $n1 \cdot n2 \cdot n3$. This implies that the computational cost heavily relies on the total number of k-points. For instance a dense grid of $4 \times 4 \times 4$ grid will require more central processing unit (CPU) time than a less dense grid of $2 \times 2 \times 2$. Obviously, a dense grid predicts better results for ground state properties, but one must seek to balance between the accuracy of the results and the computational costs. The size of the unit cell largely determines how dense the k-point grid must be. In this case, the total number of k-points is inversely proportional to the size of the unit cell, because the size of the Brillouin zone is the same as the size of the reciprocal lattice unit cell. The convergence of k-point mesh($ni \times ni \times ni$, where ni=1,2,3.....) with respect to total energies (for the cubic defect zinc-blende structure of the C_3N_4) is shown in the Figure 3.2.

3.7.3 Pseudopotentials. Atoms are made of the deep-core and valence electrons. The core electrons are highly localised and difficult to expand their wave functions within the plane wave basis set. One may argue that since core electrons do not participate in the chemical bonding, they should be completely disregarded. However, disregarding core electrons affects the orthogonality between the core states and valence state, a prime condition that must be satisfied always. As stated earlier, numerical implementation of the Kohn-Sham equations are based on various approximations. The pseudopotential is one such an approximation where, the real atomic potential is replaced by artificial potentials that mimics the core and valence states [85–88]. The use of pseudopotential in calculations has clear advantage over full-potential methods, since computational costs are reduced significantly [89–91]. Generally, pseudopotentials are not unique, and hence the results of any electronic structure calculations depend on them. Typical families of pseudopotential are norm-conserving, ultra-soft and projector augmented wave (PAW) type of

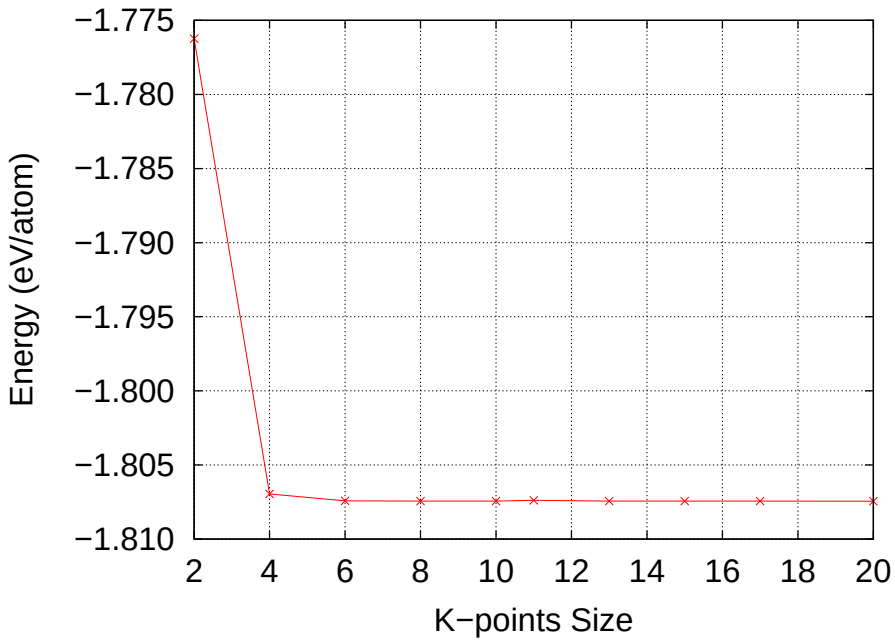


Figure 3.2 Convergence of Total Energy with k-point.

pseudopotentials [92–96].

3.7.4 van der Waals. Though DFT has been successful in predicting structural properties of bulk solids, the method fails to properly describe the weak van der Waals forces prominent in layered structures. Several density functionals with nonlocal correlations have been developed to account for those van der Waals corrections. Fundamental papers on van der Waals corrections and their implementations in various modern *ab initio* packages are found in these references [97–101]. In this thesis the van der Waals interactions described by Grimme [101] has been employed to study layered materials.

3.8 Dielectric constants

The linear response of a material to an external time-varying electric field is described by the frequency-dependent dielectric tensor $\varepsilon(\omega) = \varepsilon_1(\omega) + i\varepsilon_2(\omega)$. A dielectric tensor $\varepsilon(\omega)$ is a second rank tensor whose elements are given as ε_{xx}, ε_{yy}, ε_{zz}, ε_{xy}, ε_{xz} and ε_{yz}. The subscripts x, y and z corresponds to x, y and z axis in three dimensional.

$$\varepsilon(\omega) = \begin{vmatrix} \varepsilon_{xx} & \varepsilon_{xy} & \varepsilon_{xz} \\ \varepsilon_{yx} & \varepsilon_{yy} & \varepsilon_{yz} \\ \varepsilon_{zx} & \varepsilon_{zy} & \varepsilon_{zz} \end{vmatrix}.$$

The dielectric tensor is symmetrical, and hence for the off-diagonal elements find that $\varepsilon_{xy} = \varepsilon_{yx}$, ε_{xz}=ε_{zx} while ε_{yz}=ε_{zy}. The calculated dielectric constant is related to the experimentally available complex refractive index by $\tilde{n} = n + i\kappa = \sqrt{\varepsilon}$. In isotropic crystals like c-C_3N_4 the dielectric tensor reduces to three identical diagonal elements, which makes the dielectric constant effectively a scalar quantity. g-C_3N_4 phases are uniaxial anisotropic crystals. Here the dielectric tensor has two different diagonal values. The axis orthogonal to the layer plane is the optical axis, and its dielectric constant is denoted $\varepsilon_{\parallel}(\omega)$. The in-plane axes share identical values and their dielectric constant is denoted $\varepsilon_{\perp}(\omega)$. The imaginary part for each sampled frequency is determined by summing over terms that depend on oscillator strength and transition energies ($\omega = \epsilon_{c,k} - \epsilon_{v,k}$ which are weighted by the transition probability $\langle u_{c\mathbf{k}+\mathbf{q}e_\alpha} | u_{v\mathbf{k}} \rangle$ [102].

$$\begin{aligned} \varepsilon_2^{\alpha,\beta}(\omega) = \frac{4\pi^2 e^2}{\Omega} \lim_{q\to 0} \frac{1}{q^2} \sum_{v,c,\mathbf{k}} 2\mathrm{w}_{\mathbf{k}} \delta(E_{c\mathbf{k}} - E_{v\mathbf{k}} - \omega) \\ \times \langle u_{c\mathbf{k}+\mathbf{q}e_\alpha} | u_{v\mathbf{k}} \rangle \langle u_{v\mathbf{k}} | u_{c\mathbf{k}+\mathbf{q}e_\beta} \rangle, \end{aligned} \tag{3.8.1}$$

where the indices v and c stand for the valence and conduction band state respectively, μ_{ck} is the cell periodic part of the orbitals at k while α and β are Cartesian components. .

The corresponding real part may be obtained by Kramers-Kronig transformation [103].

$$\varepsilon_1^{\alpha,\beta}(\omega) = 1 + \frac{2}{\pi} P \int_0^\infty \frac{\varepsilon_2^{\alpha,\beta}(\omega')\omega'}{\omega'^2 - \omega^2 + i\eta} d\omega'. \tag{3.8.2}$$

For the rest of thesis, the imaginary and real parts of dielectric constant are described by the symbols ε_2 and ε_1 respectively, dropping the indices α and β.

3.9 Absorption coefficient

The frequency dependent absorption, or attenuation, coefficient $\alpha(\omega)$ describes the intensity loss per unit length (e.g. $I(x) = I_0 \exp(-\alpha x)$) and is given by [104]

$$\alpha(\omega) = \frac{2\omega}{c}\kappa(\omega) = \frac{2\omega}{c}\Im(\sqrt{\varepsilon(\omega)}) = \frac{4\pi\kappa(\lambda)}{\lambda}, \tag{3.9.1}$$

where $\kappa(\omega)$ is often called the extinction coefficient which is the imaginary part of the complex refractive index, c is the speed of light and $\lambda = \frac{2\pi c}{\omega}$ is the wave length of light. From Eq.(3.9.1) we can see that $\alpha(\omega)$ will strongly resemble $\varepsilon_2(\omega)$, but the explicit ω dependence will cause increased high-energy absorption.

3.10 Reflectivity

The reflectivity $R(\omega)$ of a material can be easily derived from its complex refractive index and the incidence angle with the Fresnel equations, which for normal incidence reduces to

$$R(\omega) = \left|\frac{\tilde{n}(\omega) - 1}{\tilde{n}(\omega) + 1}\right|^2 = \left|\frac{n(\omega) + i\kappa(\omega) - 1}{n(\omega) + i\kappa(\omega) + 1}\right|^2. \tag{3.10.1}$$

3.11 Electron energy loss spectra

The electron energy loss spectrum L(ω) describes the kinetic energy loss of an electron beam propagating through the electron gas of the medium. Naturally L(ω) has a maximum at the plasma frequency of the electrons, where a resonance occurs. Therefore, maxima in the electron energy loss function are also interpreted as plasmon resonances. The electron energy loss spectrum is given by

$$L(\omega) = \Im[\varepsilon^{-1}] = \varepsilon_2(\omega)/[\varepsilon_1^2(\omega) + \varepsilon_2^2(\omega)]. \tag{3.11.1}$$

3.12 Local field effects

The local field is that quantity which determines the polarization of the electron. It is obtained by averaging the microscopic field over the region occupied by the electron, the contribution to the average being greater from those parts of the unit cell where the electron is more easily polarized [105]. The effects of the local fields on dielectric constant are usually significant depending on the polarization of the unit cell under consideration.

4. Computational results and discussion on C_3N_4

This chapter provides a comprehensive compilation of the stability, phase transition pressures, elastic and optical properties of some phases of C_3N_4. In addition, the influence of the DFT band gap problem on the optical data is addressed.

4.1 Computational details and structural properties

The VASP code and PAW potentials [57, 58, 93, 96] are used for all calculations performed in this work. We employed the LDA functional [62, 106] to describe the exchange correlation potential. A cut-off energy of 600 eV for the plane wave basis was used for all cubic phases, and 700 eV cut-off for the layered phases.

The Monkhorst-Pack [83] k-mesh was chosen individually for the purpose of geometry optimisation and for the calculation of optical properties to ensure best results. The values used in the optical calculations are listed in Table 4.1, together with the lattice constants of the unit cells used.

The van der Waals interaction is the dominant force determining the inter-layer separation in the layered systems. LDA-DFT itself does not (properly) account for this effect and overestimates the inter-layer separation. We used the Grimme's method [98] for van der Waals corrections as included in VASP to account for that. All current van der Waals corrections for DFT are only approximate and therefore the Grimme method tendentiously underestimates the layer separation.

The layered phases are basically made of two layers per unit cell forming an AB stacking. Omitting the van der Waals corrections in calculation of lattice parameter leads to an increased layer separation, while in-plane cell parameters and atomic positions are only marginally affected. This observation was made in the layered hexagonal and rhombohedral C_3N_4 structures, where the calculated inter-layer separations of $2.82\,\text{Å}$ ($3.03\,\text{Å}$ without van der Waals corrections), which is considerably shorter than the $3.35\,\text{Å}$ of graphite. The melon structure has a layer separation of

Table 4.1 Computational details for diamond and C_3N_4. Given are the number of atoms per unit cell, the size of the k-space mesh, the lattice parameter (a,c) in Å and the cohesive energy in eV/atom. For graphitic structures: Values without van der Waals corrections (Grimme's method) in brackets.

		atoms	k-mesh		a	c	E_{coh}
Diamond	$F_{d\bar{3}m}$	2	19/19/19		3.53		-9.09
Cubic	$I_{\bar{4}3d}$	28	17/17/17	5.58	5.38		-9.13
Def. zinc-blende	$P_{\bar{4}2/m}$	7	19/19/19	5.67	3.41		-9.10
Spinel	$F_{d\bar{3}m}$	56	11/11/11	5.34	6.69		-8.12
Hexagonal	$P_{\bar{6}m2}$	14	15/15/11	8.41	4.72 (4.73)	5.63 (6.06)	-9.42
Melon		28	15/15/13	8.51	7.04 (7.06)	5.49 (5.84)	-9.45
Rhombohedral	R_{3m}	21	15/15/13	8.38	4.72 (4.73)	8.46 (9.10)	-9.42

2.74 Å (2.92 Å), and a slightly higher cohesive energy than the other structures of C_3N_4. The A-B stacked melon structure shows different structural parameters than the results of Xu and Gao [107], who used a different geometry.

4.2 Phase transition pressure

Phase stabilities of C_3N_4 are studied by calculating total energies at fixed volumes and then analyse the energy-volume and pressure-volume relationships. The analysis is based on the 3^{rd}-order Birch-Murnaghan equation of states [108], whereby the fitted energy-volume data yields the equilibrium lattice parameters shown in Table 4.1. The energy versus volume plot for various phases of C_3N_4 are shown in Figure 4.1. The layered phases including the hexagonal, rhombohedral, buckled and melon structures are the most energetically favourable compared to the spinel, cubic and def. zinc-blende phases.

To understand phase stabilities at high pressure, we have to fall back on the Gibbs free energy (G) [19]. It is defined as G = E+PV-TS, where P stand for pressure, V denote volume while T and S represent temperature and entropy respectively. Fundamentally, DFT calculations are performed

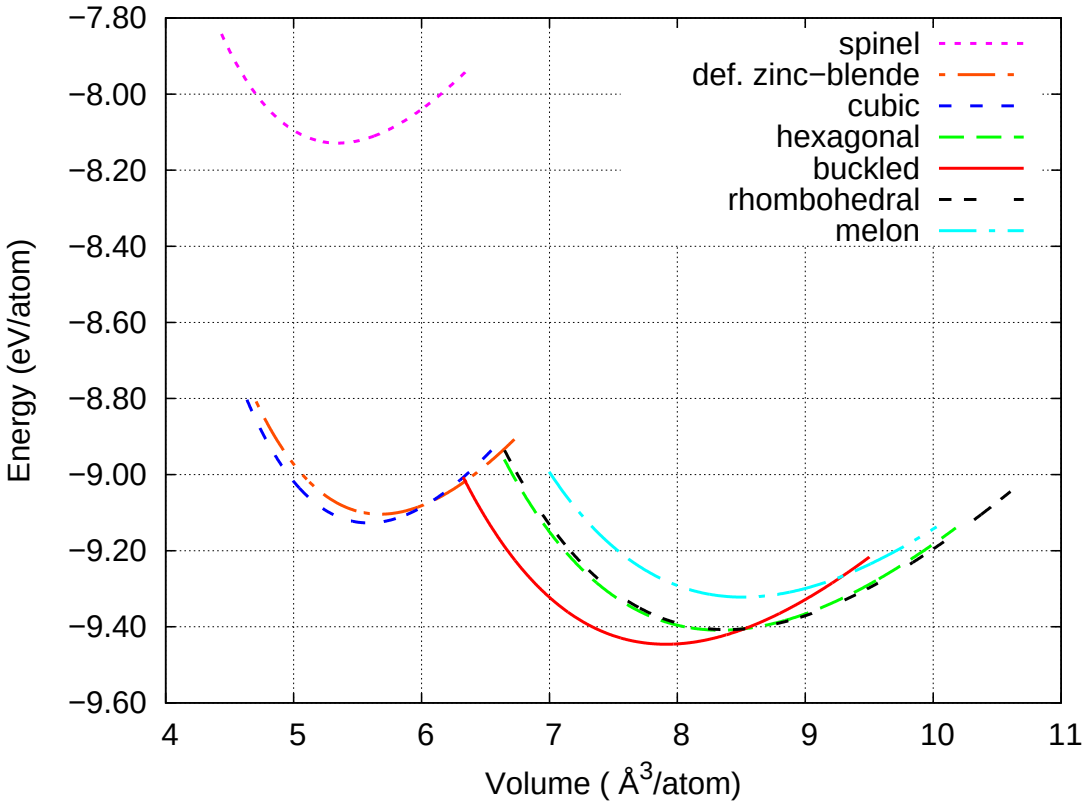


Figure 4.1 Total energy (eV/atom) versus volume/atom $V_0(Å^3)$ for various phases of C_3N_4.

at zero temperature, thus the Gibbs free energy can be equated to the enthalpy H=E+PV. It is inferred from Figure 4.1 that structures with small volumes per atom are favourable at high pressure [109]. Transformations from low pressure crystal structures to high pressure structures is governed by the fundamental thermodynamic principles that no two phases can exist over a given range of pressure. Hence, the transition pressure from one phase to another is simply the point where phase curves cross each other. The pressure-enthalpy relationships shown in Figure 4.2 suggests that the layered structures are likely to transform into the non-layered structures. Such transformation from the layered phase to non-layered phase is well known in the phase diagram of carbon that involves graphite and diamond. The transition pressure from hexagonal phase to cubic phase is about 17 GPa slightly above the 12 GPa obtained by Teter et al. [18]. The discrepancy here may be attributed to structural differences as a result of the van der Waals correction.

The hexagonal $\rightarrow$ cubic transition is a companied by the decrease in the volume by 34%. The

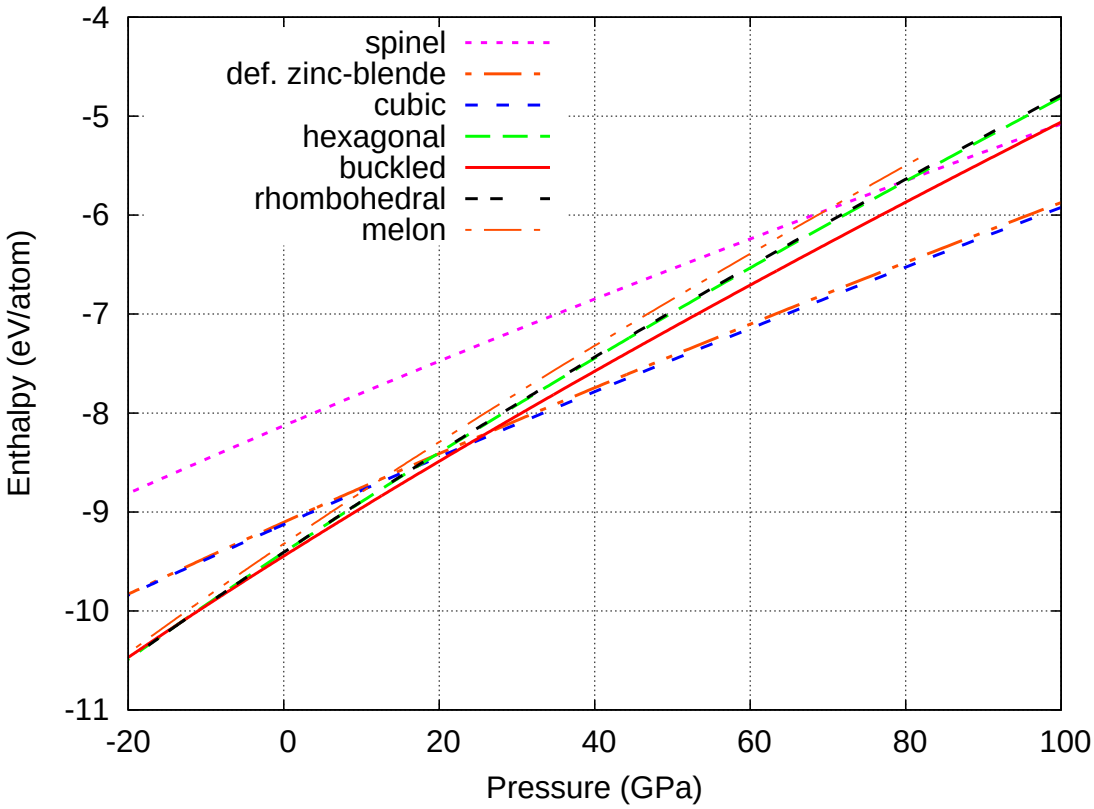


Figure 4.2 The pressure-enthalpy curves for various phases of C_3N_4.

layered hexagonal phase is also a potential precursor for the synthesis of the def. zinc-blende phase, though a pressure of about 19 GPa would be required for such transformation to take place. Huge amount of pressure of about 80 GPa would be needed to transform the hexagonal layered phase into a non-layered spinel phase. The volume reductions in the hexagonal $\rightarrow$ def. zinc-blende and hexagonal $\rightarrow$ spinel transformations are 33% and 36% respectively.

If the mechanically stable buckled geometry based on the rhombohedral C_3N_4 is considered, the transition pressures would be as follows; buckled $\rightarrow$ cubic (23 GPa), buckled $\rightarrow$ def. zinc-blende (26 GPa) and buckled $\rightarrow$ spinel (98 GPa). Overall, transitions pressures from the layered structures to the competing tetrahedrally coordinated cubic and def. zinc-blende phases differ slightly and both phases can be recovered at low pressures unlike the spinel structure, which would require a pressure range of 60-100 GPa.

4.3 Elastic properties of C_3N_4

As mentioned in previous chapters, there are many ways of describing the hardness of a material. The most obvious way is to correlate hardness to elastic properties. Therefore, accurate determination of the elastic tensor and evaluation of its coefficients is crucial for quantifying hardness of a material. The computed independent elastic constants for different phases of C_3N_4 are listed in Table 4.2. For layered systems, the van der Waals interaction is accounted for using the Grimme's method [101]. The cubic structures are characterised of having large values of elastic constants while the weak forces that holds the graphene-like sheets together prevent the layered phases from attaining large out-of plane elastic constants. Taking the example of hexagonal phases, the value of c_{33} with inclusion of the van der Waals corrections is thrice the value without van der Waals corrections.

Table 4.2 Computed elastic constants c_{ij} (GPa) for various C_3N_4 phases. For graphitic phases, elastic constants (in brackets) are obtained by inclusion of van der Waals interaction.

Compound	c_{11}	c_{33}	c_{44}	c_{12}	c_{13}	c_{14}
Diamond	1097,1060[c]		595,562[c]	150,125[c]		
Def. zinc-blende	865,840[a]		467,452[a]	221,213[a]		
Cubic	861,863[a]		469,348[b]	300,313[b]		
Spinel	536		539	395		
Hexagonal	803	34	5	166	-3	
	(904)	(111)	(12)	(181)	(-9)	
Rhombohedral	772,870[a]	43,57[a]	6,14[a]	235,148[a]	-2,-3[a]	0,1[a]
	(910)	(107)	(10)	(156)	(-8)	
Buckled	(714)	(81)	(9)	(113)	(35)	

[a]Ref. [11], [b]Ref. [18], [c]Ref. [110]

Derived elastic properties i.e, the elastic bulk modulus B(GPa), shear modulus G(GPa), G/B ratio, Young's modulus E(GPa), Poisson's ratio ν and predicted Vickers hardness H_v are listed in Table 4.3. The non-layered structures are predicted to be potential candidates for superhard materials, given that all of them show high resistance to change in shape and low compressibility.

To compute the Vickers hardness of C_3N_4 phases, the semi-empirical model H_v=2(G^3/B^2)$^{0.585}$-3 is adopted which relies on the values of shear (G) and bulk (B) modulus. For the sake of

Table 4.3 First principles results for elastic bulk modulus B(GPa), shear modulus G(GPa), G/B ratio, Young's modulus E(GPa), Poisson's ratio ν and predicted Vickers hardness H_v. The experimental values are in brackets.

Compound	B	G	G/B	E	ν	H_v
Diamond	466	546	1.1	1178	0.08	93(96[a])
Def. zinc-blende	436	409	0.9	935	0.14	60
Cubic	487	393	0.8	930	0.18	48
Spinel	442	352	0.8	834	0.19	44
Hexagonal	249	194	0.8	462	0.19	30
Rhombohedral	245	198	0.7	469	0.18	31
Buckled	208	152	0.7	215	0.25	23

[a]Ref. [111]

comparison, the computed H_v=93 GPa of diamond is in agreement with the experimental value of H_v=96 GPa [111]. The metastable def. zinc-blende phase have H_v=60 GPa, whereas the H_v for the cubic and spinel phases are predicted to be 48 GPa and 44 GPa respectively. The differences in H_v between the cubic and def. zinc-blende, introduces the debate on the relationships between hardness and B or G. The facts emerge that cubic phase have larger bulk modulus but smaller shear modulus than both def. zinc-blende and diamond. This observation leads to a conclusion that shear modulus is a good indicator of hardness of the material. While this argument holds for this particular compound, it cannot be generalized to other materials, which have to be treated case by case.

4.4 Optical properties of C_3N_4

FIG. 4.3 shows the real part of the dielectric function of c-C_3N_4 and g-C_3N_4 polymorphs. FIG. 4.4 shows the corresponding imaginary parts. The computed real and imaginary parts of the dielectric

function of diamond are compared with the experimental data from literature [8]. The redshift of both the real and imaginary parts of the dielectric function is caused by the underestimate of electronic band gap within DFT. The calculated dielectric function For diamond-like structures, the dielectric tensor has only one independent component. However, for graphitic structures the dielectric tensor is anisotropic, hence we show both components parallel and perpendicular to the optical axis. The dielectric functions correspond to a Lorentzian inter-band transition model as expected of semi-conductors/insulators.

As can be seen from FIG. 4.4 all three cubic structures show significantly different behaviour. The cubic structure has two prominent Lorentz peaks around 8 eV and 13.5 eV, which is not unusual for semi-conductors [112]. The defect zinc-blende structure has far greater resemblance with the diamond dielectric function, showing only one prominent peak at abound 13 eV. Nevertheless, it has a broad left flank, which might indicate the existence of a lower energy peak, not revealed by the DFT simulation. The spinel structure shows one peak around 7 eV. Such an extremely asymmetric form is rather unusual. As the plateau region is on the higher energy flank it can not be explained with the same argument as for defect zinc-blende case.

The g-C_3N_4 share very similar dielectric functions, which resemble the graphite dielectric function. In all cases the perpendicular component shows a prominent peak around 3-4 eV, commonly accounted to π electrons and a broader peak around 14-15 eV from the σ electrons. In the melon phase this second maximum is much less pronounced and almost completely smeared out. The parallel component is overall very weak as graphitic structures contain mostly vacuum in this direction. In the optical and near ultraviolet there is very little absorption and an almost constant real part.

For the sake of comparison a slightly distorted "buckled" phase derived from the rhombohedral phase is included. The buckling leads to a smearing of the dielectric function, but no physical change in the main features. Therefore, basing the calculations on the unstable perfect planar unit cells does not disturb the results, within the limits of accuracy one can achieve with the methods at hand. Omitting the van der Waals corrections basically leads to an increased layer separation while in-plane cell parameters and atomic positions are marginally affected. As can be seen in FIG. 4.3 and FIG. 4.4 the changes in the dielectric function are small. In the limit of the

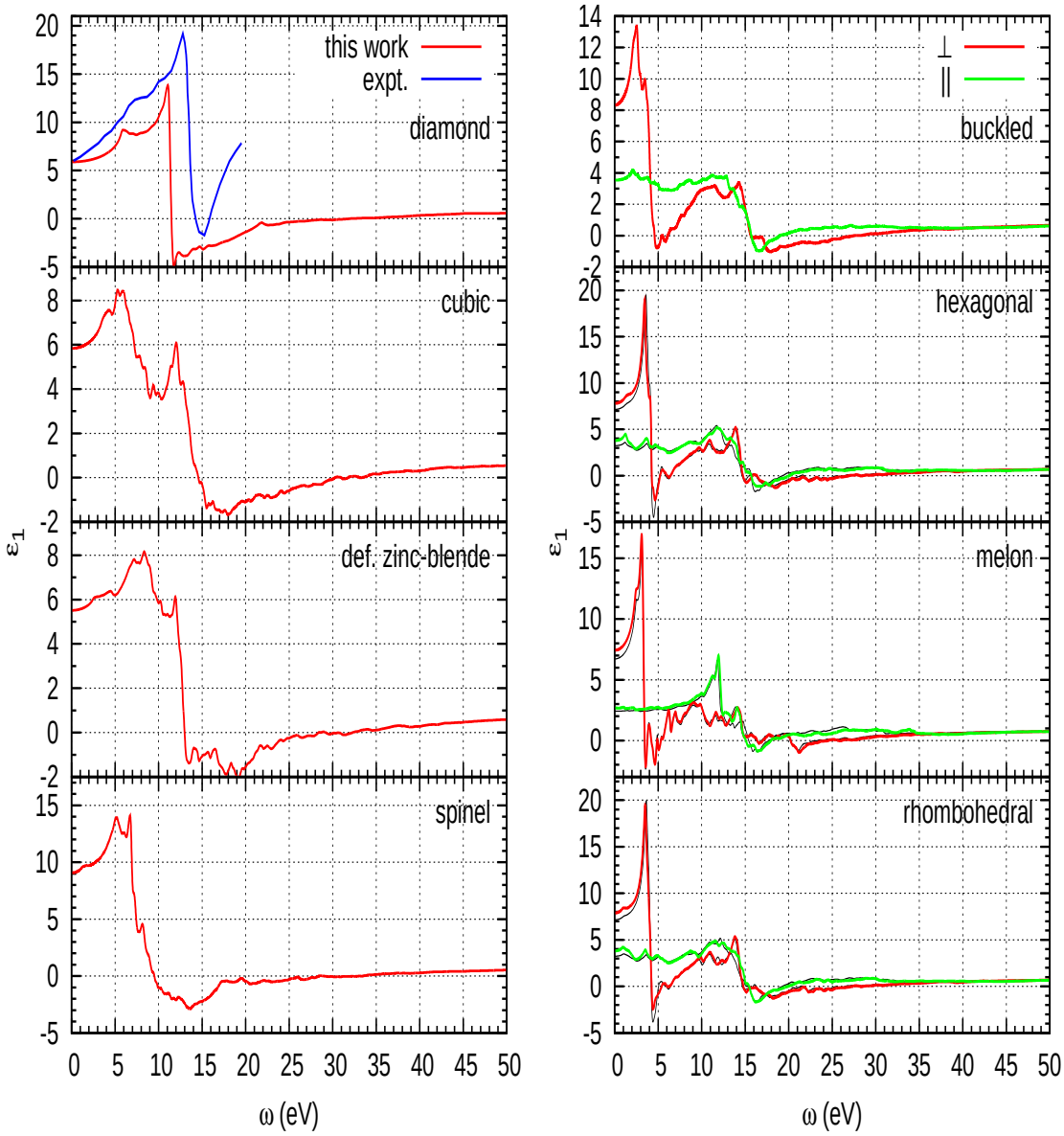


Figure 4.3 Real part of frequency-dependent dielectric function for diamond and several polymorphs of C_3N_4. For graphitic phases: Values without van der Waals correction has narrow black lines. The experimental (expt.) data for diamond was obtained from Ref. [8].

static dielectric constant the values without van der Waals interaction are consistently smaller. The increased layer separation increases the cell volume, which reduces the dielectric constant, if everything else stays the same. For the rest of the thesis only results including van der Waals corrections are presented for g-C_3N_4.

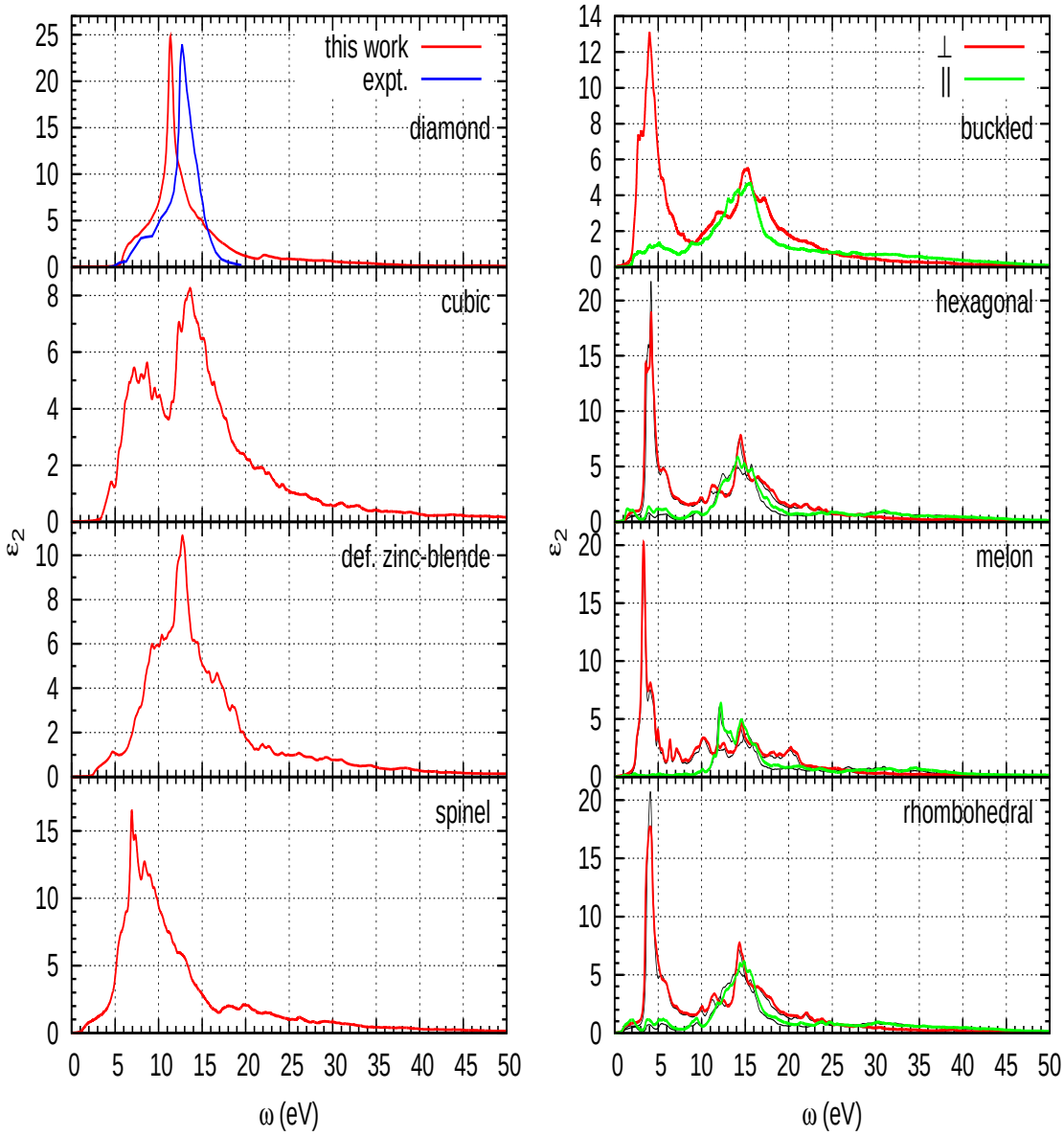


Figure 4.4 Imaginary part of frequency-dependent dielectric function for diamond and several polymorphs of C_3N_4. For graphitic phases: Values without van der Waals correction has narrow black lines. The experimental (expt.) data for diamond was obtained from Ref. [8].

In the limit of $\omega = 0$ one can use density functional perturbation theory [102, 113, 114] instead of the linear response ansatz. This usually yields much better results, as ε_∞, the static macroscopic dielectric constant in the long wave length limit, is a ground state property and does not depend of the band gap. It is also possible to leave the independent particle model and include local

Table 4.4 Ion clamped static macroscopic dielectric constants ε_∞ and the ionic contribution ε^{ion} are calculated using DFPT method. ε_∞^{-lf} represents value without inclusion of local field effects while ε_∞^{+lf} represent those values with local field effects. The ionic contributions are given by ε^{ion}. For g-C_3N_4 the values of ε_∞ are reported as $\varepsilon_\perp/\varepsilon_\parallel$. The free electron plasma-frequency ω_p (eV) is shown as well.

	ε_∞^{+lf}	ε_∞^{-lf}	ε^{ion}	ω_p
Diamond	5.83	5.96		34.3
Cubic	5.83	6.01		33.8
Def. zinc-blende	5.25	5.52		32.5
Spinel	8.58	9.09		25.5
Hexagonal	7.07 / 3.45	7.83 / 3.81	2.83 / 0.37	
Melon	7.50 / 3.25	8.65 / 3.56	2.94 / 1.65	
Rhombohedral	7.14 / 3.48	7.89 / 3.84	2.77 / 0.38	

field effects. The static macroscopic dielectric constant obtained by use of the density functional perturbation theory is usually a convenient starting point for the convergences of conduction bands needed in the equations 3.8.1 and 3.8.2.

The static macroscopic dielectric constant with and without local field effects is listed in Table 4.4 together with the free electron plasma frequency. Our predicted ε_∞ for def. zinc-blende structure is 5.25, which is in good agreement with 5.19 predicted by Hu et al. [115]. However, for spinel structure we predict a value of 8.58 which is higher than 7.7 reported by Mo et al. [34] and 6.27 reported by Hu et al.. The local field effects reduce the static dielectric constant, only little for c-C_3N_4, but a lot more for g-C_3N_4. Especially the perpendicular component for the melon structure is reduced drastically by 45%.

For photon energies in the infrared and below a significant amount of the dielectric response comes from the ions. The ionic contributions ε^{ion} add to give the total static constant $\varepsilon_0 = \varepsilon_\infty + \varepsilon^{ion}$. The ionic contributions in the limit of $\omega = 0$ are listed as well in Table 4.4.

As soon as the dielectric function, or the complex refractive index, is known, other optical properties of materials like reflectivity/reflectance, absorption, etc. may be extracted.

4.5 Derived optical properties

4.5.1 Absorption coefficient. The calculated absorption coefficients are given in FIG. 4.5. C_3N_4 shows absorption of up to 0.3 nm^{-1}. Again the similarity of hexagonal and rhombohedral g-C_3N_4 is very strong. The two phases mainly differ by a different stacking (A-B v.s A-B-C) which seems to be largely irrelevant for the optical properties. The structural difference between triazine and heptazine building blocks is much more important. The c-C_3N_4 structures show the expected features already discussed for the dielectric function, which resemble diamond much in form and strength of the absorption spectrum.

4.5.2 Reflectivity. FIG. 4.6 shows the reflectivity of diamond and the C_3N_4 structures. In the visible spectrum the c-C_3N_4 structures have relatively low reflectivities between 16 % and 25 % in the $\omega = 0$ limit, and it slowly increases with energy similar to diamond. The spinel structure is the most reflective structure. Reflectivity increases until it reaches the maximum in the ultraviolet, between 7 eV and 20 eV, depending on the structure. The maximum reflectivities is around 40 % to 48 %. For energies above 20 eV the reflectivities are decreasing and they reach zero in the high energy limit, the materials become optically transparent. The g-C_3N_4 reflectivities strongly follows the π and σ peaks leaving areas of low reflectivity in between, and a minima around 8 eV. The melon structure differs from the other layered structures by an increased reflectivity in an area around 15 eV. The parallel component shows reflectivities of less than 5 % for the optical spectrum.

4.5.3 Electron energy loss. Diamond and all c-C_3N_4 structures show a single maximum at the corresponding plasma frequencies around 34 eV to 36 eV, as shown is FIG. 4.7. The calculated ω_p of diamond (34.3eV) agrees well with the value obtained experimentally [8, 116]. Triazine based g-C_3N_4 show a maximum around 31 eV for the perpendicular component. The heptazine structure has the same maximum located around 28 eV. A smaller maximum around 6-7 eV accounts for π plasmons in all g-C_3N_4. This is very similar to the graphite electron energy loss spectrum [117]. The parallel components do not show clear maxima, which makes it impossible to extract a plasma frequency for the electron energy loss spectrum.

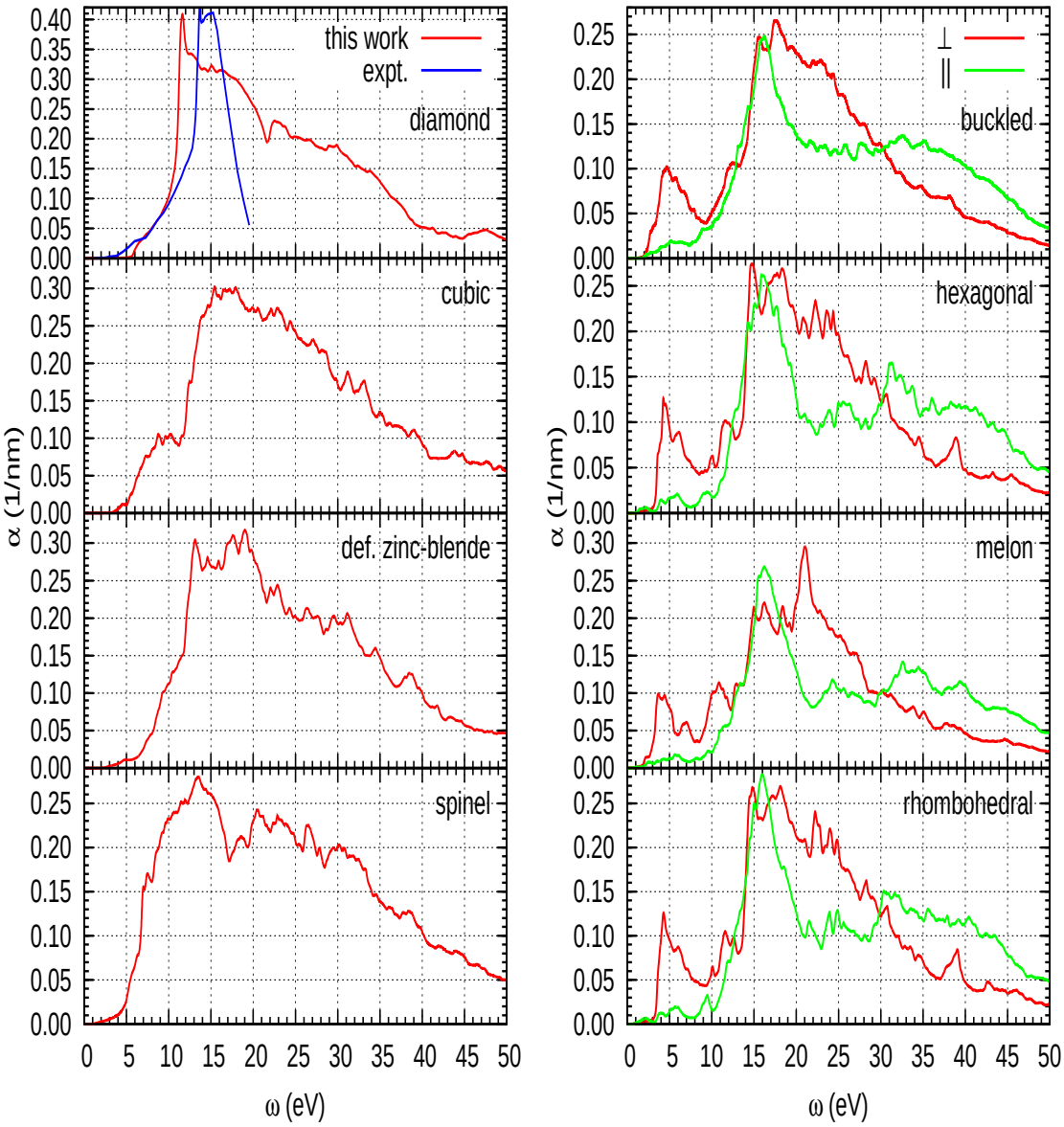


Figure 4.5 Absorption spectrum of the frequency-dependent dielectric function for diamond and several polymorphs of C_3N_4. The experimental (expt.) data for diamond was obtained from Ref. [8].

4.6 Density of states and band gap

Though density functional theory (DFT) within the local density approximation and generalised gradient approximation(GGA) continue to play an important role in predicting ground state properties of materials, the band gap problem remains a major challenge. The DFT Kohn-Sham

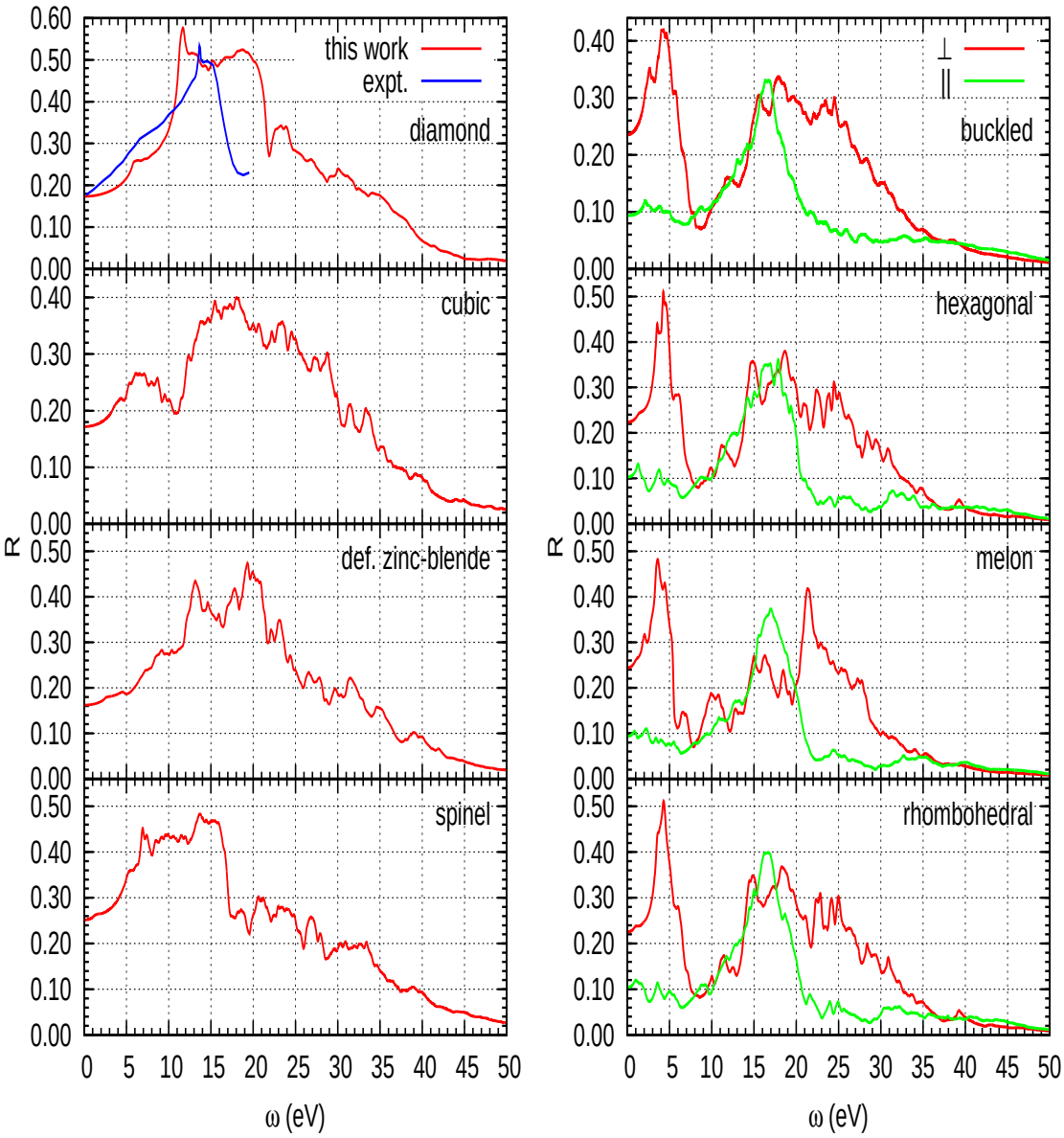


Figure 4.6 Reflectivity spectrum of frequency-dependent dielectric function for diamond and several polymorphs of C_3N_4. The experimental (expt.) data for diamond was obtained from Ref. [8].

gap (E_g-KS) is the difference between eigenvalues of lowest unoccupied and highest occupied eigenstates. Reasons for underestimation may be partly due to delocalization error or lack of derivative discontinuity in the exchange-correlation potentials [118, 119]. In recent years, attention has been paid to the development of new density functionals, so-called hybrid functionals to correct the band gap problem. Furthermore, the GW approximation [78] which takes into account

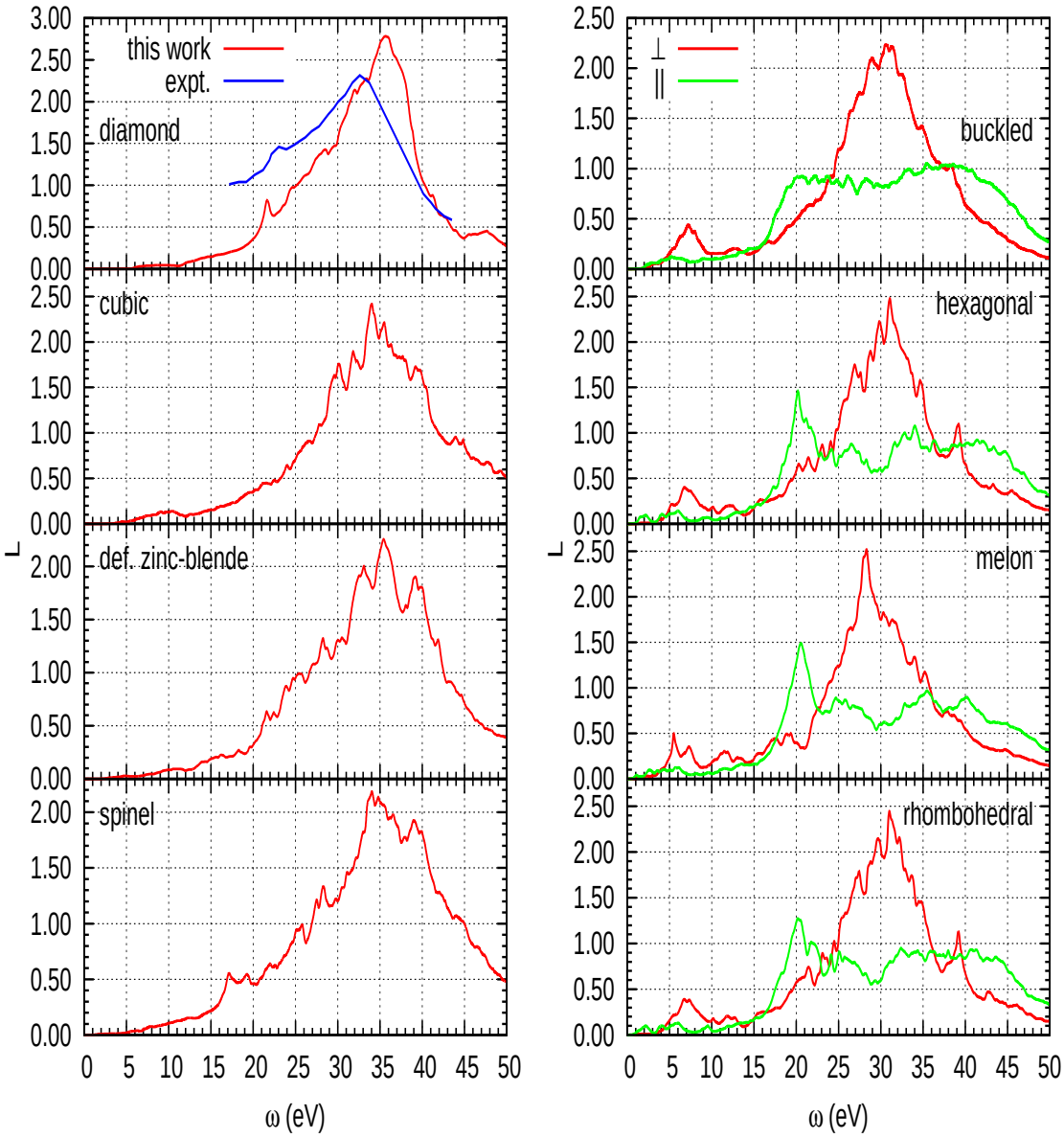


Figure 4.7 Electron energy loss spectra of the frequency-dependent dielectric function for diamond and several polymorphs of C_3N_4. The experimental (expt.) data for diamond was obtained from Ref. [8].

the electron-electron(e-e) interactions has of late been prescribed as a state-of-the-art method for predicting accurate band gaps. The GW approximation is however limited to compounds with small number of electrons in the unit cell. Luckily, one does not necessary need to perform a full self consistent GW calculations to obtain the band gap close to experimental value. Instead one may choose a non-self-consistent approach, the so-called G_0W_0 approach [120], in which neither

the quasi-particle energies nor the quasi-particle wave functions are updated.

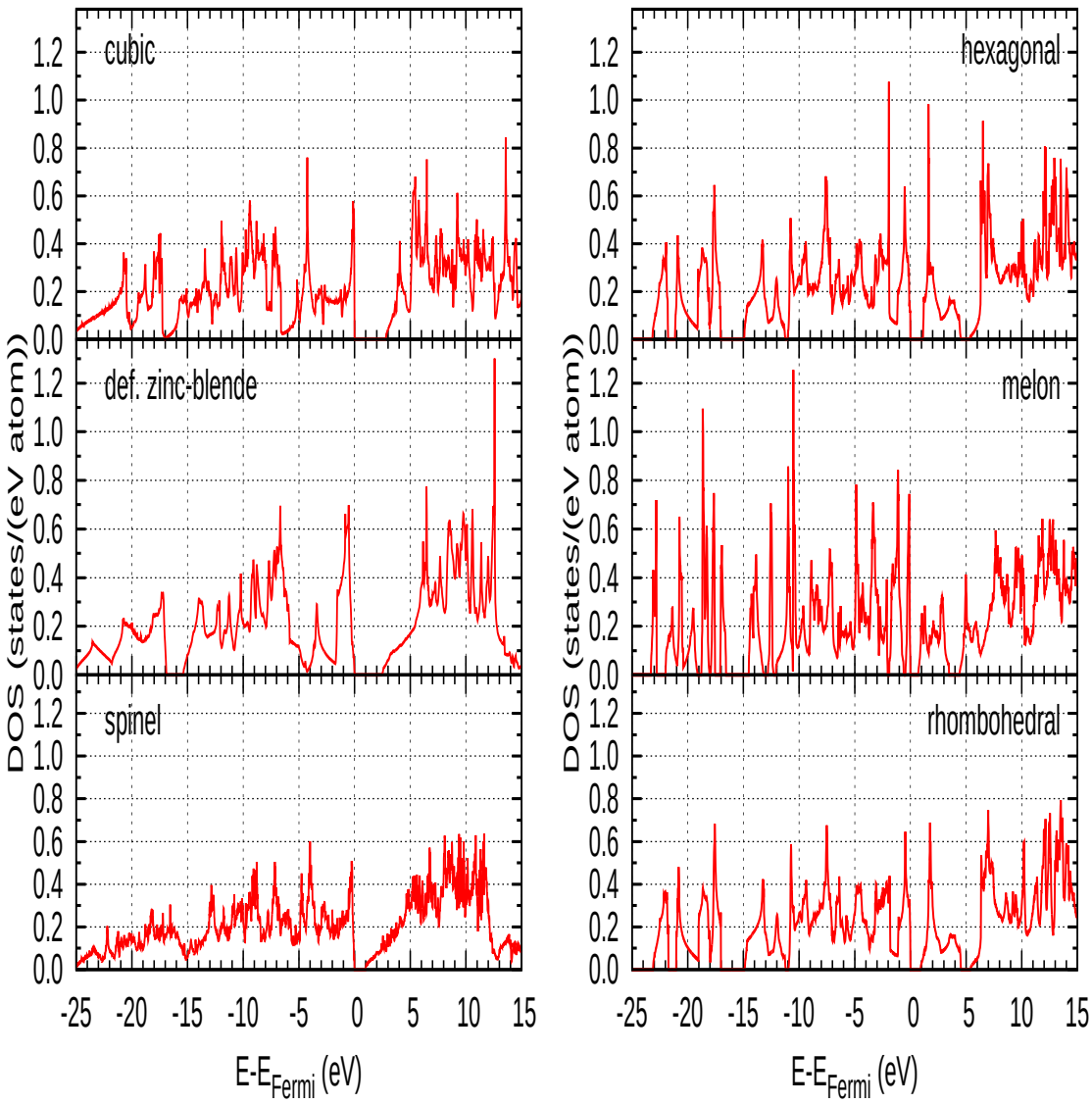


Figure 4.8 Density of states for several polymorphs of C_3N_4 obtained using LDA. The Fermi level is set to the highest occupied band energy.

A comparison of the calculated band gap using various exchange-correlation functionals for some phases of C_3N_4 is shown in Table 4.5. Note that the conventional exchange correlations i.e LDA and GGA predict small band gaps. Slight improvements are achieved when the Tao-Perdew-Staroverov-Scuseria (TPSS) [75] exchange-correlation functional are used. Calculations of band

Table 4.5 Calculated energy band gap (eV) for several polymorphs of C_3N_4 calculated with different methods. Direct (d) and indirect(i) band gaps are indicated.

	LDA	PBE	HSE	TPSS	MBJ
Cubic	2.90(i)		4.45(i)	3.22(i)	4.69(i)
Def. zinc-blende	2.68(d)		4.70(d)	2.94(d)	4.57(d)
Spinel	1.02(i)		2.28(i)	0.99(i)	2.09(i)
Hexagonal	1.15(i)	1.27(i)	2.75(i)	1.44(i)	2.74(i)
Melon	0.71(i)				
Rhombohedral	0.90(i)	1.01(d)	2.41(d)	1.16(d)	2.50(d)

gaps beyond LDA and GGA are tedious especially when hybrid functionals like HSE06 [76,77] are used. The computational resources needed and the computation time required for the HSE06 calculations depend on the size of the system, the cut-off energy of the plane waves and the *k*-points grid. An alternative method is to use the modified Becke-Johnson (MBJ) potentials [79, 80]. The HSE06 and MBJ methods predict similar results as listed in Table 4.5, yet MBJ will require minimal computational resources compared to HSE06. The density of states obtained from the LDA calculations is shown in Figure 4.8. The Fermi level is set to zero, which also serve as the highest occupied molecular orbital (HOMO). The gap above HOMO but below the lowest unoccupied molecular orbital (LUMO) corresponds to the differences in the valence band maximum and conduction band minimum shown in Table 4.5.

4.7 Summary

In summary, this chapter was intended to provide a comprehensive study of the stability, phase transformations and general structural, elastic, electronic and the frequency dependent optical properties of various polymorph of C_3N_4 by calculating the complex dielectric function. The study of optical properties has been emphasized as it fills a gap in the existing literature on C_3N_4. The predicted plasmon peaks and the refractive index of the compounds studied here will be useful

data for experimentalists that attempt to synthesize C_3N_4. It has also been illustrated in Table 4.4 that the static dielectric constants are sensitive to local fields effects. The wide band gap of the cubic C_3N_4 and def. zinc-blende C_3N_4 are interesting for applications in semiconductor technology.

5. Computational results on carbon dinitrides (CN_2)

The focus of this chapter is to illustrate the concept of predicting new materials by utilizing existing crystallographic databases and DFT simulations in order to predict novel materials. As a rule of thumb, one needs to have the knowledge of the atomic structure to perform DFT calculations. For materials with known experimental structures, DFT calculations are straightforward. However, in the situation where no known experimental structures are available, one chooses hypothetical starting configurations, and then proceeds with computer experiments exploring possible stable configurations.

Seven crystal structures described by their space group symbols are considered in this chapter: space group $Cmc2_1$ denoted as cmc21-CN_2, space group $P\bar{3}m1$ denoted as p3m1-CN_2 and space group $P\bar{4}2_1m$ denoted as pc-CN_2. Further, space group $I\bar{4}2d$ is denoted as bct-CN_2, space group $I\bar{4}2m1$ denoted as I42m-CN_2, space group $Pa\bar{3}$ denoted as pa3-CN_2 and space group Pbam denoted as pbam-CN_2.

5.1 Energy versus volume

An equation of state for a solid is a useful thermodynamical concept that has been widely adopted to describe energy-volume and pressure-volume relationships from low to very high pressures. Pressure is a thermodynamic variable that can be easily explored in the first-principles calculation of minimum energy at ground state. In this work, self-consistent calculations of the total energy of CN_2 were performed for each crystal structure at a set of seven different volumes ranging from $V/V_t =$ 0.94 to 1.06. Where V_t is an equilibrium volume obtained from either previous calculation or an educated guess. Those volumes were held constant while all ions were allowed to relax. The computed energy-volume data were then fitted to the commonly used 3^{rd}-order Birch-Murnaghan equation of states [108], to extract equilibrium lattice parameters, volume per atom V_0(Å^3), bulk moduli B_0 (GPa) and derivatives of the bulk modulus B_0' as listed in Table 5.1.

Table 5.1 Calculated lattice constants a, b and c (Å), volume/atom V_0(Å^3), gravimetric density (gcm^{-3}), and bulk mudulus B_0 (GPa), derivatives of the bulk modulus B_0' and Cohesive energy E_{coh} (eV).

Compound	atoms	k-mesh	a	b	c	V_0	ρ	B_0	B_0'	E_{coh}
pc-CN_2	6	14/14/13	3.316	3.316	4.752	8.709	2.54	161	2.89	-8.023
bct-CN_2	24	4/4/5	6.475	6.475	3.434	6.015	3.69	400	3.99	-7.820
p3m1-CN_2	6	13/13/8	2.365	2.365	10.70	8.644	2.56	184	3.63	-7.791
cmc21-CN_2	12	10/6/7	2.480	6.439	4.582	6.109	3.62	372	3.72	-7.682
14m2-CN_2	6	13/13/9	2.469	2.469	3.63	6.091	5.99	401	4.11	-7.658
pbam-CN_2	24	7/4/3	2.381	8.257	8.258	6.777	3.27	259	4.07	-7.497
pa3-CN_2	12	13/13/13	4.049	4.049	4.049	5.533	4.00	328	5.39	-6.796

Note that the accuracy of the DFT calculations rely upon the choice of the functional used as well

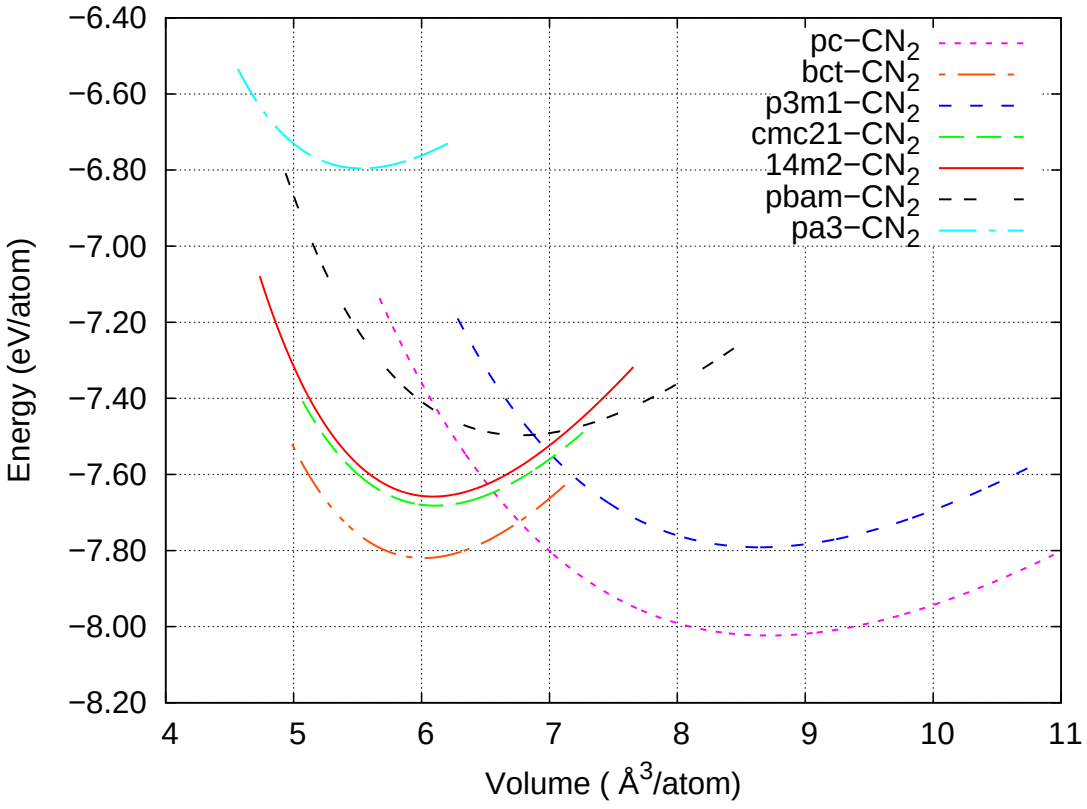


Figure 5.1 The total energy (eV/atom) versus volume/atom V_0(Å^3) for various phases of CN_2.

as on the input structure configurations. In this case, the generalized gradient approximation was intentionally deployed to alleviate the overbinding of lattice parameter prominent in local density approximation [62, 106]. The cohesive energies summarized in Table 5.1, point to pc-CN_2 as the the most stable structure in agreement with the previous calculations [45]. Figure 5.1 shows the plot of energy versus volume for seven predicted phases of CN_2. These figures are quite informative since they provide the much needed information on the relative stabilities of the CN_2 polymorphs. The energetically most stable structure pc-CN_2 deviates from the high-energy phase by 1.2 eV. The cmc21-CN_2 and I42m-CN_2 phases show degeneracy in their structural energy,

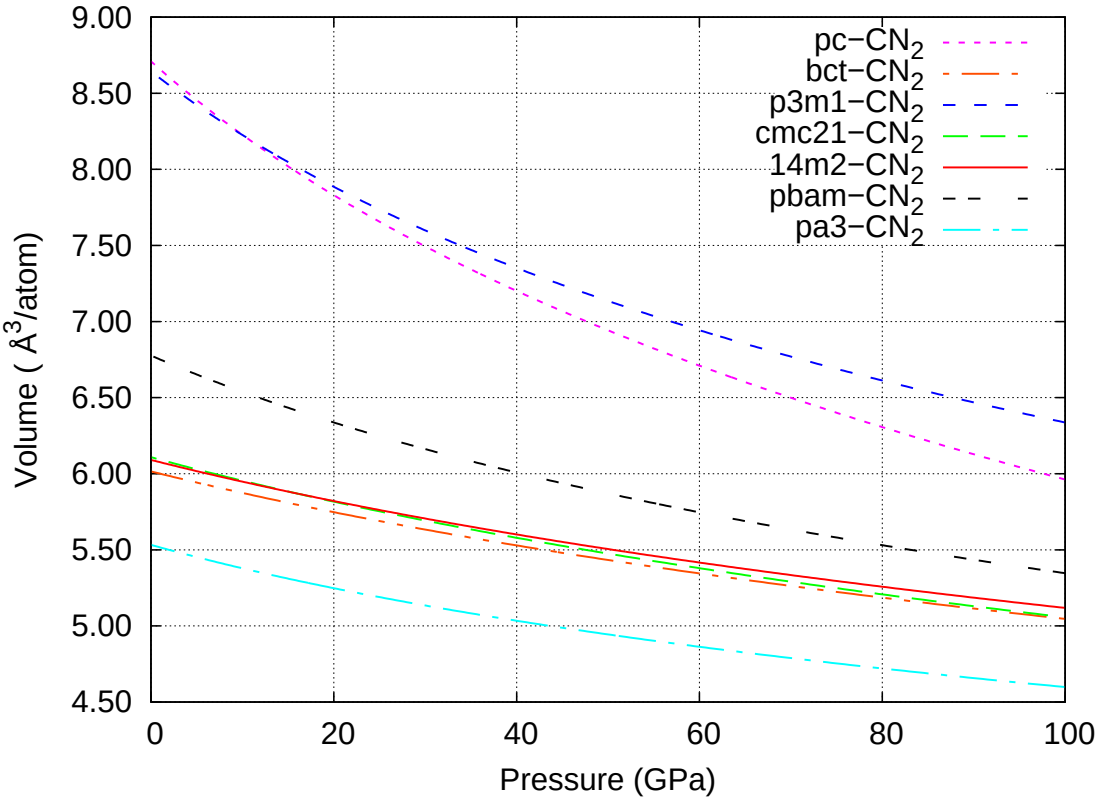


Figure 5.2 The volume-pressure curves for various phases of CN_2. Volume decrease with increasing pressure and therefore pc-CN_2 phase is the zero-pressure stable structure.

which lies about 0.34 eV above pc-CN_2, the most stable phase.

The bulk modulus B_0 is a property of material that quantifies the amount of resistance against change of volume when pressure is uniformly exerted on the material. Low compressible materials have large bulk moduli and hence high resistance to volume change. The CN_2 phases can be

categorized into three ranges of bulk moduli. First, phases with B_0 below 200 GPa (phases with low resistance to volume change) are p3m1-CN_2 and pc-CN_2. They form layered structures with hexagonal cells. The weak van der Waals forces that hold the adjacent layers together are responsible for the low B_0. Furthermore, the p3m1-CN_2 and pc-CN_2 phases are also characterised by wide and almost flat energy curves, an indication that the two phases are highly compressible compared to any other structures. The second range of B_0 is the one with values ranging between 200-300 GPa. These are phases with medium resistance to volume change. The pbam-CN_2 phase with a simple orthorhombic cell belongs to this category. The third category includes phases with B_0 above 300 GPa. These phases have high resistance to volume change. Their B_0 can be compared to the 442 GPa of diamond. Phases in this category are the base-centred orthorhombic cmc21-CN_2, the I42m-CN_2 with a simple tetragonal unit cell, the base-centred tetragonal bct-CN_2 and the pa3-CN_2 phase with a simple cubic structure. Theses phases also exhibit very high gravimetric density compared to other phases. Most solids [121] have their B_0' approximately equal to 4. In the case of CN_2, B_0' is around 4 for most phases with the exception of pc-CN_2 and pa3-CN_2 phases, where B_0' is 2.89 and 5.39 respectively.

5.2 Phase Transition

Derived quantities of the energy-volume relationships are significant in the range of zero to high pressures. The enthalpy equation G = E+PV-TS, is significant in understanding the thermodynamics of one phase with respect to the other. From the enthalpy equation and Figure 5.2 structures with small volumes per atom are favourable at high pressure. As pointed out before, transformations from low pressure crystal structures to high pressure structures are governed by the corollary of thermodynamics that no two phases exist over given range of pressure. The transition pressure from one phase to another is obtained at the point of intersection of the enthalpy-pressure plots as displayed in Figure 5.3. The low pressure phase of CN_2 is the pc-CN_2 structure, which remains stable for the range of pressure below 13.24 GPa, before transforming into bct-CN_2 structure as shown in Figure 5.4(a). This transformation leads to a decrease in volume by 31% and an increase in gravimetric density ρ of about 45%. Furthermore, the tran-

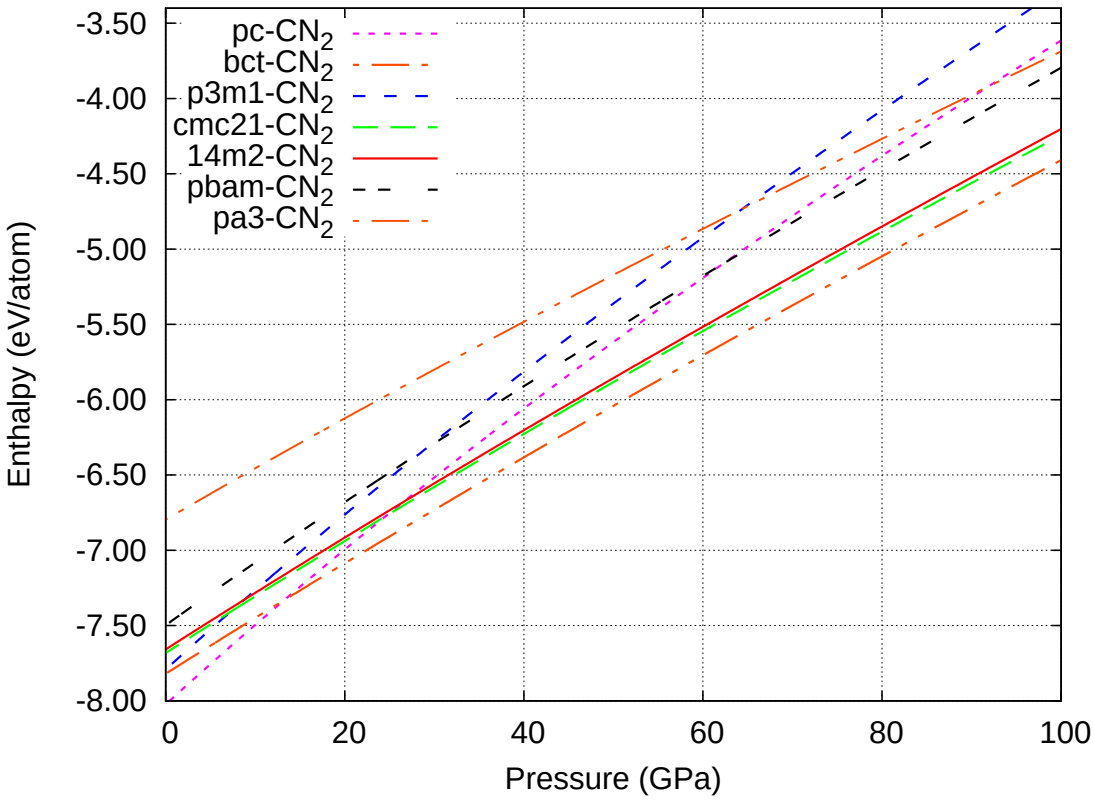


Figure 5.3 Plot of enthalpy versus pressure obtained by fitting energy-volume data to EOS. The crossover between any two lines is interpreted as the transition pressure from one phase to another.

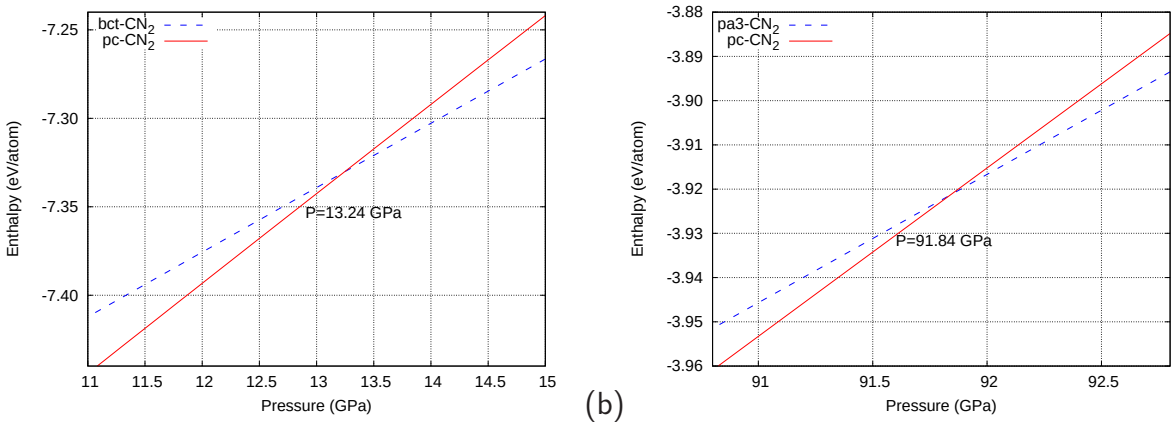


Figure 5.4 Phase transition pressure (a) P=13.24 GPa for pc-CN_2 $\rightarrow$ bct-CN_2 and (b) P=91.84 GPa for pc-CN_2 $\rightarrow$ pa3-CN_2.

sition pressure from low pressure pc-CN_2 to very high pressure phase pa3-CN_2 was predicted to be 91.84 GPa, as shown in Figure 5.4(b). The volume reduction and increment in ρ was de-

termined to be about 36% and 57% respectively. The transformation from pc-CN_2 to pa3-CN_2 can also be achieved when pc-CN_2 transforms into other intermediary high pressure phases. The predicted transition pressure from pc-CN_2 to cmc21-CN_2 is 24.19 GPa as shown in Figure 5.5(a). This phase change leads to a decrease in volume by 29%, while the change in density is up to 42%. From the two scenarios, a trend is already established whereby high-pressure phases can be recognised by their small volumes and high densities.

There is no rule on how volumes and densities change with respect to each other. One such case is when pc-CN_2 transform to I4m2-CN_2 phase at transition pressure of about 26.36 GPa as displayed in Figure 5.5(b). This transformation is accompanied by a change of volume of about 30% and a drastic increase in ρ.

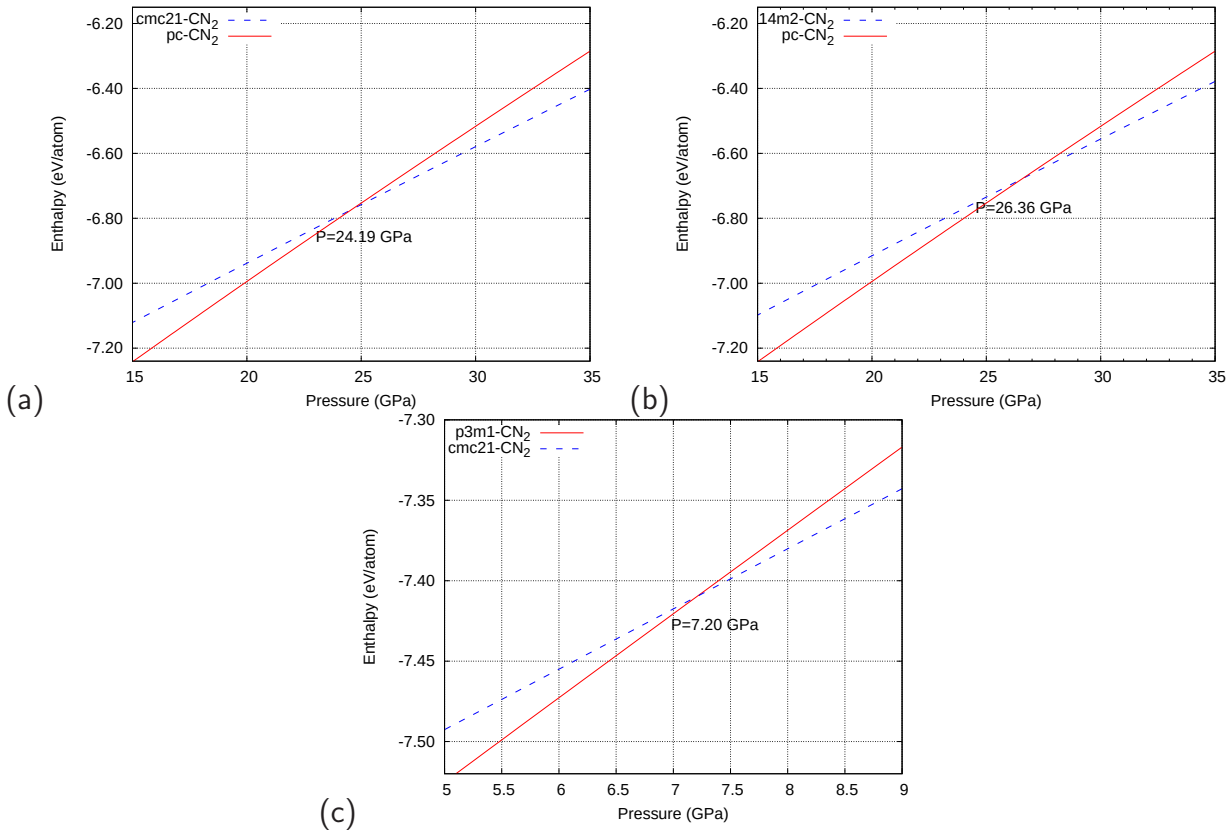


Figure 5.5 Phase transition pressure (a) P=24.19 GPa for pc-CN_2 $\rightarrow$ cmc21-CN_2, (b) P=26.36 GPa for pc-CN_2 $\rightarrow$ I4m2-CN_2 and (c) P=7.20 GPa for p3m1-CN_2 $\rightarrow$ cmc21-CN_2.

Other phase transformations are observed when a p3m1-CN_2 is compressed. This structure is

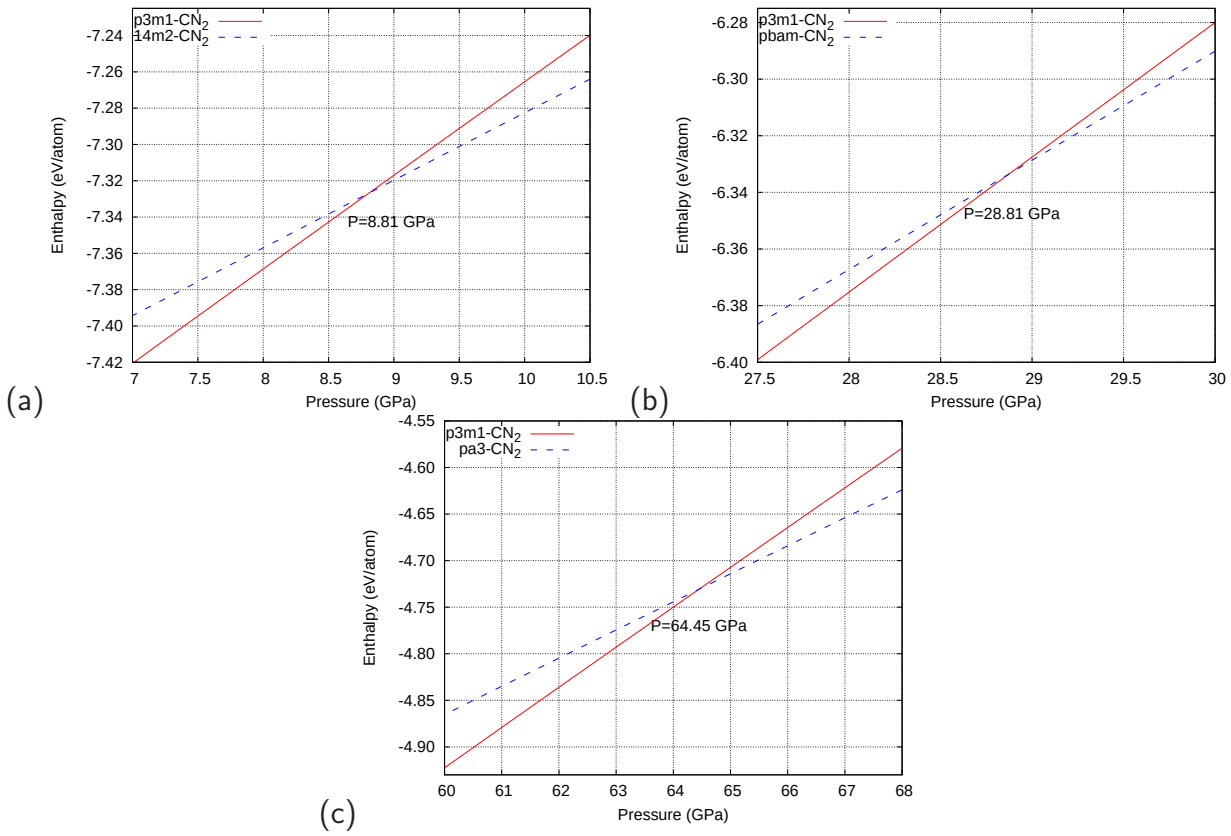


Figure 5.6 Phase transition pressure (a) of P=8.81 GPa for p3m1-CN_2 → I4m2-CN_2, (b) P=28.81 GPa for p3m1-CN_2 → pbam-CN_2 and (c) P=64.45 GPa for p3m1-CN_2 → pa3-CN_2.

slightly higher in energy than pc-CN_2 phase. The p3m1-CN_2 phase is only 0.02 gcm^{-3} denser and offers slightly more resistance to volume change than pc-CN_2. The transition pressures for the p3m1-CN_2 → cmc21-CN_2 transformation is 7.20 GPa as shown in Figure 5.5(c). Here, the volume reduction and density increment is 29% and 41% respectively. It also requires a small pressure of about 8.81 GPa for p3m1-CN_2 → I4m2-CN_2 transition to occur (see Figure 5.6(a)). The structural energy of the two phases differ by 0.133 eV, only that I4m2-CN_2 is more resistant to volume change.

It requires a pressure of about 28.81 GPa (shown in Figure 5.6(b)) for p3m1-CN_2 → pbam-CN_2 transition. The energy differences in the two phases is a small fraction of an eV, and only a small change in volume of about 21% and density of 27% is reported. Furthermore, a transition pressure of 64.45 GPa (shown in 5.6(c)) is required for the p3m1-CN_2 → pa3-CN_2 phase change.

Such transformations will lead to a drastic reduction in volume by 35%, and increase in density by 57%.

5.3 Summary

The present work has revealed that CN_2 exists in numerous stable phases in a pressure range of 0-100 GPa. It has been noted that energies in cmc21-CN_2 and I42m-CN_2 are degenerate though I42m-CN_2 is very dense and the least compressible phase of CN_2. The layered pc-CN_2 phase is energetically favourable at low pressure, while pa3-CN_2 is a higher energetic structure occurring at high pressures. Under compression, the pc-CN_2 phase transforms into several high pressure phases i.e pc-CN_2 $\rightarrow$ pbam-CN_2, and pc-CN_2 $\rightarrow$ cmc21-CN_2 accompanied with volume reduction and increment in density. The pc-CN_2 $\rightarrow$ I4m2-CN_2 transition is characterised by a small change in volume and but huge increase in the density. The pc-CN_2 $\rightarrow$ bct-CN_2 transformation leads to 31% decrease in volume and only 45% increase in density. Large volume reduction of 36% is observed in pc-CN_2 $\rightarrow$ pa3-CN_2 transition whereby the change in density is up to 57%.

6. Comparative studies of CN_2, SiN_2 and GeN_2 compounds

In the previous chapter, CN_2 with space group $Cmc2_1$ was identified as one of the high pressure phases with large bulk moduli. A new strategy is devised whereby the, carbon(C) in the CN_2 compound is substituted with some of the other elements in group IV i.e silicon(Si) and germanium(Ge). This method has successfully been used to predict both silicene and germanene [46] from the graphene [14] structure. DFT calculations are performed to compare various electronic structural properties of CN_2, SiN_2 and GeN_2. The choice of the orthorhombic structure of space group $Cmc2_1$ (shown in Figure 6.1), which is a prototype structure of copper silver sulphide (CuAgS) [122], was made based on the fact that it is mechanically stable and can be adopted by all three compounds i.e CN_2, SiN_2 and GeN_2. These compounds serve as a good example of isostructural compounds, a template that can be used to demonstrate the process of data mining based on electronic structure calculations.

Further motivation in this work, is derived from the computational discoveries of C_3N_4, Si_3N_4, Ge_3N_4 and Sn_3N_4 [17,123,124] that were eventually validated by experiments [20,125,126]. Note that despite the prediction of the tetrahedrally coordinated β-C_3N_4 forming the basis of recently discovered compounds like spinel Si_3N_4, Ge_3N_4 and Sn_3N_4, there has not been any successful synthesis of its crystalline form.

By investigating the electronic and structural properties of CN_2, SiN_2 and GeN_2, the strength and the weakness of some functionals used in DFT are highlighted. In particular, a comparison is made on the outcomes of the LDA, PBE and PBESol functionals for structural optimization, and on the HSE06 hybrid functional and modified Becke-Johnson (MBJ) potentials for determining the electronic band gap [62,68–70,76,77,79,80,106]. As usual, optimization of cut-off energies (600 eV) and *k*-point grid (10x6x7) was performed prior to calculating equilibrium properties. For optical properties, a dense *k*-point grid of 14x10x11 and a high energy cut-off of 900 eV were used.

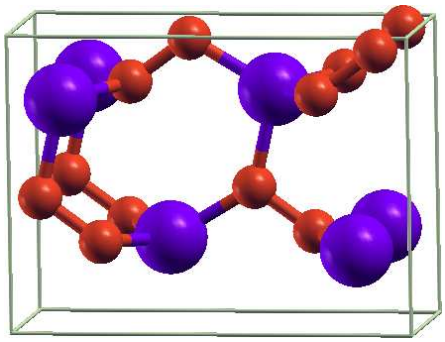


Figure 6.1 The base centered orthorhombic space group $Cmc2_1$ (No. 36) adopted by XN_2, where X= C, Si and Ge. The blue (large spheres) and red (small spheres) represent X and N respectively.

6.1 Equilibrium structural properties

As a test case, structural relaxation of CuAgS compound were performed using LDA, PBE and PBESol, and compared to the outcome to the experimental data of Baker et al. [122]. The computed equilibrium lattice parameters are listed in Table 6.1. It is clear that PBEsol, an exchange correlation functional that was parametrized specifically for solids, yields results that agree well with the experimental data. The tendency of LDA to overbind and PBE to underbind is quite noticeable in the calculated lattice parameters of CuAgS. Similar trends are observed in the lattice parameters of CN_2, SiN_2 and GeN_2. The equilibrium volumes per atom and the gravimetric densities are shown in Table 6.1. Due to overbinding of lattice constants in LDA, the predicted volume of CuAgS is about 7% less than the experimental value. Consequently, the predicted gravimetric density ρ is about 11% larger than experimental value. As seen in Table 6.1, PBE predicted larger volumes and hence lower gravimetric densities, while volume and gravimetric density determined using PBEsol do not heavily deviate from the experimental values. The comparison of calculated results for CN_2 with other theoretical calculations is satisfactory, while for SiN_2 and GeN_2 the present results can be used as reference for future experimental and computational works.

It is understood that the atomic radius of the elements in the periodic table increases down the group. The volumes increases in the order $CN_2 < SiN_2 < GeN_2$, while gravimetric densities ρ need not follow this format because the increase of mass and the binding lengths are different.

Table 6.1 Calculated lattice constants a, b and c (Å), gravimetric density (gcm^{-3}), and volume V (Å^3). A comparison between experimental and other theoretical studies is also shown.

Compound	Exchange-correlation	a (Å)	b (Å)	c (Å)	ρ(gcm^{-3})	V (Å^3)
CN_2	LDA	2.445	6.381	4.518	3.76	70.50
	PBE	2.480	6.439	4.582	3.62	73.18
	PBEsol	2.461	6.413	4.546	3.70	71.78
	Other[a]	2.481	6.441	4.584	3.62	73.25
SiN_2	LDA	2.916	7.421	5.100	3.37	110.40
	PBE	2.959	7.490	5.175	3.24	114.75
	PBEsol	2.937	7.463	5.136	3.30	112.61
GeN_2	LDA	3.124	7.628	5.416	5.17	129.12
	PBE	3.226	7.681	5.684	4.74	140.91
	PBEsol	3.157	7.684	5.467	5.03	132.64
CuAgS	LDA	3.944	6.493	7.793	7.00	199.68
	PBE	4.059	6.670	8.114	6.22	219.72
	PBEsol	3.953	6.605	8.010	6.58	209.19
	Expt[b]	4.059	6.617	7.967	6.32	213.97

[a]Ref. [45], [b]Ref. [122]

6.2 Mechanical and Dynamic Stability

The mechanical stability for CN_2, SiN_2 and GeN_2 was determined by checking the signs of the independent elastic constants. For the orthorhombic structure, the independent components of the elastic tensor matrix in Voigt notation [127] are the six diagonal elements c_{11}, c_{22}, c_{33}, c_{44}, c_{55}, and c_{66} and three off-diagonal elements c_{12}, c_{13} and c_{23}. All these materials meet mechanical stability criteria; $c_{11} + c_{22} + c_{33} + 2(c_{12} + c_{13} + c_{23}) > 0$, $c_{11} + c_{22} - 2c_{12} > 0$, $c_{11} + c_{33} - 2c_{13} > 0$, $c_{22} + c_{33} - 2c_{23} > 0$, as derived by Born [128].

The computed independent elastic constants are shown in Table 6.2. Values obtained using LDA are larger than the PBE results, due to overbinding respectively underbinding of the lattice

Table 6.2 A comparison of independent elastic constants (GPa units) obtained using LDA, PBE and PBEsol.

Compound	Exchange-correlation	c_{11}	c_{22}	c_{33}	c_{12}	c_{13}	c_{23}	c_{44}	c_{55}	c_{66}
CN_2	LDA	966	1270	866	34	96	165	470	286	183
	PBE	872	1193	785	25	92	141	438	266	178
	PBEsol	925	1234	830	29	93	149	458	273	179
SiN_2	LDA	469	668	93	89	63	158	254	73	74
	PBE	442	610	133	75	58	133	237	76	71
	PBEsol	453	639	89	83	59	151	247	71	73
GeN_2	LDA	332	481	129	77	44	146	178	35	52
	PBE	260	350	145	40	22	94	138	45	44
	PBEsol	306	445	122	66	38	135	168	30	49

constants. The LDA calculated elastic constants for CN_2 are smaller than those reported for cubic C_3N_4 and diamond [2].

6.3 Derived elastic properties

There exists a distinct relationship between elastic constants and several fundamental physical properties of solids such as elastic bulk modulus. It is also common practice to relate the shear and Young's moduli and Poisson's ratio to elastic constants. The bulk modulus [129] (also known as incompressibility) is a ratio that relates an applied constant stress to the fractional volumetric change. Both SiN_2 and GeN_2 are highly compressible, and softer than the low compressible CN_2. The compressibility of these materials rely upon the strength of the covalent bonding formed between the C-N, Si-N and Ge-N. Obviously, short bond lengths are more incompressible, while longer bonds tend to be weaker and easily compressed. A comparison of bulk moduli calculated with LDA, PBE and PBEsol are recorded in Table 6.3.

LDA predicts larger bulk moduli for the three materials because of the overbinding of the lattice

Table 6.3 Derived variables of elastic constants; bulk modulus B (GPa), shear G (GPa) and Young's modulus E (GPa), shear/bulk modulus ratio (G/B), Poisson's ratio ν and Vickers hardness (H_v) GPa. H_v is calculated from a semi-empirical model H_v=2(G^3/B^2)$^{0.585}$-3.

Compound	Exchange-correlation	B	G	E	G/B	ν	H_v
CN_2	LDA	410	375	813	0.91	0.16	54
	PBE	374	349	756	0.93	0.15	53
	PBEsol	392	363	785	0.92	0.16	54
SiN_2	LDA	205	141	255	0.68	0.20	20
	PBE	191	138	277	0.72	0.20	21
	PBEsol	196	137	246	0.69	0.20	20
GeN_2	LDA	164	98	198	0.59	0.25	13
	PBE	119	85	184	0.72	0.22	15
	PBEsol	150	91	184	0.60	0.25	13

constants. PBE on the other hand, gives the smallest bulk moduli due to underbinding of the lattice constants. The calculated bulk moduli with PBEsol lie between those of LDA and PBE. The bulk and shear moduli are the key properties to search for a potential ultra-hard material.

The shear modulus relates to how a material responds to change in shape (while the volume is kept constant). GeN_2 has the least resistance to change in shape while CN_2 has greater resistance than both SiN_2 and GeN_2 (see Table 6.3). The 375 GPa shear modulus for CN_2 is very close to the 393 GPa reported for cubic C_3N_4, but far less than the 546 GPa reported for diamond [2]. This means that none of the three materials considered in this work would exceed the hardness of diamond H_v=93. Surprisingly CN_2 is about 12% harder than the cubic C_3N_4. The differences in H_v between CN_2 and cubic C_3N_4 cannot be attributed to a single calculated quantity, but rather to a combination of several factors. The most prominent and easily computed is the G/B ratio. For CN_2 the G/B ratio is higher than those of SiN_2 and GeN_2, and is about 12% greater than that of C_3N_4. This percentage is similar to the differences in the H_v of the two materials.

The Young's modulus E can be determined by combining both B and G [129]. It is associated

with the hardness of a material just like the shear modulus. As seen in Table 6.3, Young's modulus decreases from CN_2 to SiN_2 and finally to GeN_2. Based on LDA results, the Young's modulus of SiN_2 is about 31% that of CN_2, while the Young's modulus of GeN_2 is only 24% that of CN_2.

The Poisson's ratio ν is another measure of the stability of the crystal structure against shearing [129]. Calculated Poissons ratio using different exchange-correlation functionals are reported in Table 6.3. All three materials considered in this work are brittle since their ν is less than 0.33 and their G/B ratio greater than 0.5 [130].

6.4 Electronic structure

Metals, semiconductors and insulators are distinguished by the presence and size of the band gap. DFT calculations of the band gap using either local or semi-local exchange-correlation functionals are known to underestimate the experimental gap [118, 119]. More advanced, time consuming and perhaps more accurate methods for calculating fundamental and DFT band gaps are either hybrid functionals (like HSE06) [76, 77] or the GW approximation [78]. The use of hybrid functionals and GW method is quite prohibitive for large systems due to numerical efforts involved. The alternative method is the use of modified Becke-Johnson (MBJ) potentials [79,80]. The MBJ potentials are more desirable for predicting band gap since they are computationally less expensive and yet often give similar results as hybrid functionals and GW. MBJ potentials have been applied to numerous solids, and the accuracy of the obtained bad gaps has been reported to be in good agreement with experiments [131]. However, note that performance of MBJ potential in predicting band gaps is still not of the same quality as the HSE06 or GW, and also based on a weaker theoretical foundation. The calculated band gaps using LDA, PBE, PBEsol, MBJ and HSE06 are reported in Table 6.4. LDA, PBE and PBEsol underestimates band gaps by 40-70% with respect to energy gaps calculated using MBJ or HSE06. CN_2 is a direct band gap material with sufficient large energy gap that would make this material attractive as a photocatalyst in water splitting process to harvest hydrogen. Both SiN_2 and GeN_2 are characterised by an indirect band gap. Interband transitions in indirect band gap materials require extra momentum from phonons, and hence opto-electronic devices made from this material are less efficient.

Table 6.4 Calculated energy band gap (eV) for CN_2, SiN_2 and GeN_2 calculated with different methods.

Compound	LDA	PBE	PBEsol	MBJ	HSE06	Type of band gap
CN_2	1.08	1.07	1.02	2.37	2.48	direct
SiN_2	2.11	2.08	2.01	3.59	3.50	indirect
GeN_2	0.55	0.01	0.30	1.95	1.52	indirect

6.5 Optical Properties

Some of the aims of investigating optical properties are to explore materials for opto-electronic applications and to harvest of solar energy. The numerical determination of the frequency-dependent dielectric constant is limited to a linear response level, without taking into account local field effects.

The real ε_1 and imaginary ε_2 parts of the frequency-dependent dielectric function for CN_2, SiN_2 and GeN_2 calculated using PBEsol functional are displayed in Figure 6.2. Due to the orthorhombic symmetry of the unit cell, the optical spectra are different for light polarized along the three crystallographic axes. However, in the optical spectra presented in Figure 6.2 the average of the dielectric function along the three crystallographic axes is shown. In the limit of $\omega = 0$, the real part of frequency-dependent dielectric function corresponds to the static macroscopic dielectric constant ε_∞ extracted for CN_2, SiN_2 and GeN_2 as 5.76, 5.44 and 9.54, respectively. GeN_2 has almost twice the static macroscopic dielectric constant of both CN_2 and SiN_2. The high static macroscopic dielectric constant in GeN_2 was expected due to a narrow band gap compared to the rest of nitride materials studied in this work, as well as its higher density. The dielectric constants for the crystallographic axes are shown in Table 6.5.

Another approach for computing the static macroscopic dielectric constant is by use of the density functional perturbation theory (DFPT) [102, 113, 114]. The static macroscopic dielectric constants with (ε_∞^{+lf}) and without (ε_∞^{-lf}) local field effects and ionic contributions ε^{ion} to dielectric constants are listed in Table 6.5. Generally, the local field effects reduce the static dielectric

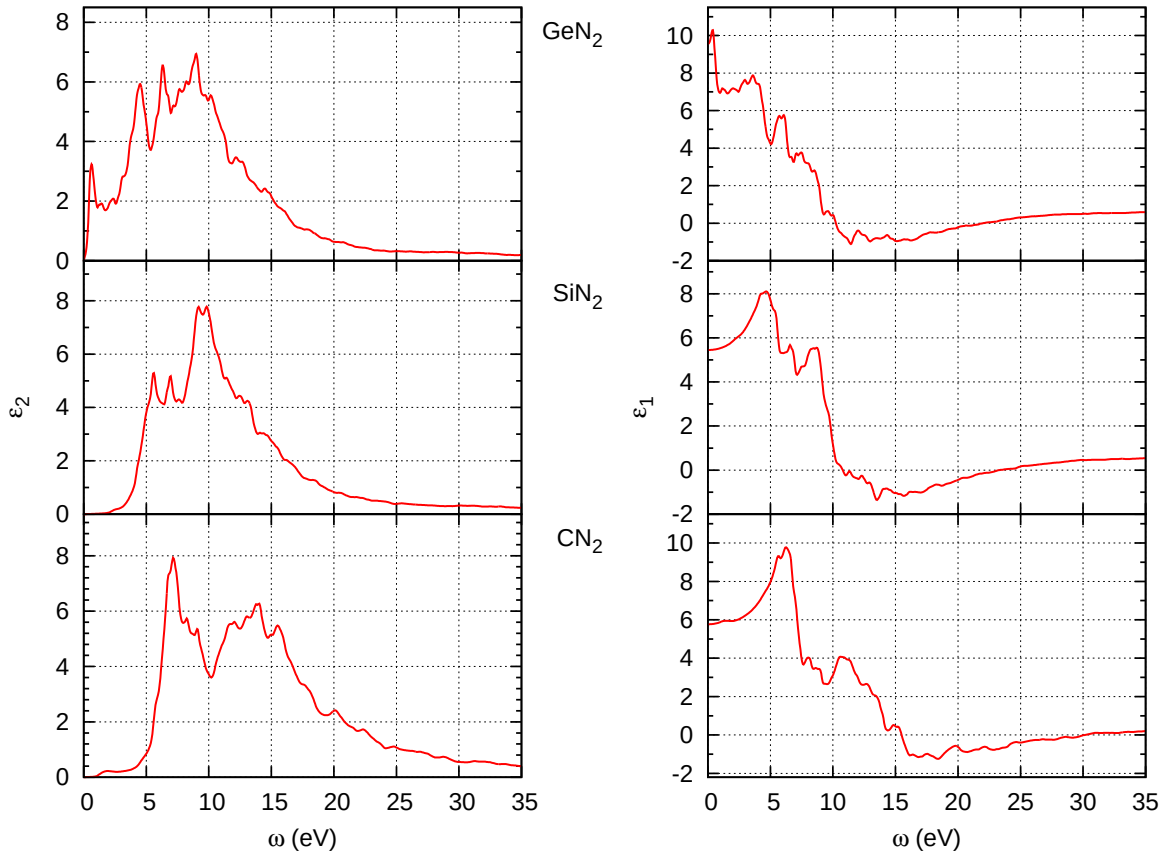


Figure 6.2 The real ε_1 and imaginary ε_2 parts of frequency-dependent dielectric function for CN_2, SiN_2 and GeN_2 calculated using PBEsol functional.

constant, although the magnitude of deviation depend upon the material and the crystallographic axes under consideration. The free electron plasma frequency denoted by ω_p (eV) may be extracted from the electron energy loss spectrum (not shown). The averaged values for ω_p are listed in Table 6.5 as well.

From the imaginary part of dielectric function, one can see a clear picture of the behaviour of optical absorption spectra. The first absorption peak for GeN_2 within the visible range was located at 0.6 eV while the rest of the peaks were within the ultraviolet range. For SiN_2, there was no absorption within visible range since the first absorption peak was located at 5.6eV deep in the ultraviolet range. On the other hand, the first absorption peak for CN_2 was located within visible range at 1.9eV. Note that for accurate calculation of absorption spectra, the excitonic interactions must be taken in account by solving the Bethe-Salpeter equation(BSE) [132]. BSE

Table 6.5 Static macroscopic dielectric constants ε_∞ and the ionic contribution ε^{ion} are calculated using DFPT. ε_∞^{-lf} represents value without inclusion of local field effects while ε_∞^{+lf} represent those values with local field effects. The free electron plasma-frequency is denoted by ω_p (eV). Only results obtained using PBEsol are presented.

	ε_∞^{+lf}			ε_∞^{-lf}			ε^{ion}			ω_p
	ε_a	ε_b	ε_c	ε_a	ε_b	ε_c	ε_a	ε_b	ε_c	
CN_2	5.14	6.12	5.63	5.21	6.30	5.78	2.30	1.00	2.89	34.0
SiN_2	4.59	5.78	5.63	4.73	5.83	5.77	4.60	2.51	9.13	24.6
GeN_2	13.02	8.05	6.61	13.49	8.39	6.74	6.18	2.45	7.49	23.1

calculations are prohibitive for large system, since they rely on the quasiparticle energies from the GW method.

6.6 Summary

This chapter has investigated some structural stabilities of CN_2, SiN_2 and GeN_2 and found that the compounds fulfil the mechanical test conditions. PBEsol predicts lattice constants that are in agreement with the experiments as in the case of CuAgS. From the band gap calculations, SiN_2 and GeN_2 are indirect band gap materials while CN_2 has a wide direct band gap. Elastic properties reveals that CN_2 is a potential ultrahard material with shear modulus of about 31% lower than that of diamond.

7. Comparative studies of nitride imides

This chapter further illustrates the process of computational material discovery and search for low-compressible and superhard materials. The progress made so far in predicting low-compressible and superhard materials based on DFT is amazing with experimental studies lagging well behind. As an example, the mechanical, structural, electronic and optical properties of $C_2N_2(NH)$, $Si_2N_2(NH)$, $Ge_2N_2(NH)$ and $Sn_2N_2(NH)$ are discussed in this chapter, and comparisons with previous studies are made. The predicted structural equilibrium properties, electronic and optical properties were performed using the generalised gradient approximation GGA, within an energy cutoff of 600 eV and Γ-centered Monkhorst-Pack grid [83] of 6x6x6.

7.1 Structural and electronic properties

To obtain relaxed structures, optimization of the ionic positions and the lattice geometry were performed, yielding the theoretically estimated lattice constants as presented in Table 7.1. Calculated lattice constants for $Si_2N_2(NH)$ and $C_2N_2(NH)$ are compared to experimental values and other previous theoretical calculations [47–49, 51]. There are no feasible experimental or theoretical values to compare with the ones calculated for $Sn_2N_2(NH)$ and $Ge_2N_2(NH)$ compounds.

Further calculations were performed to obtain total energies at different volumes. In this case, volumes were held constant while all atomic positions were relaxed for each volume. Figure 7.1 shows the energy per atom versus volume per atom curves for the four compounds. The $Sn_2N_2(NH)$ has the largest value of the volume while $C_2N_2(NH)$ has the least, due to the smaller atomic radii. The atomic radii of elements increase down the group in the periodic table.

On fitting the total energies and volume to the Birch-Murnaghan [108] equation of states, the bulk moduli was extracted as 262 GPa, 107 GPa, 62 GPa and 32 GPa for $C_2N_2(NH)$, $Si_2N_2(NH)$, $Ge_2N_2(NH)$ and $Sn_2N_2(NH)$ respectively. The bulk modulus of 262 GPa for $C_2N_2(NH)$ compares well with the measured value of 258 GPa [48]. Considering the bulk modulus as a measure of resistance against a change of volume of a material caused by an applied external pressure, both

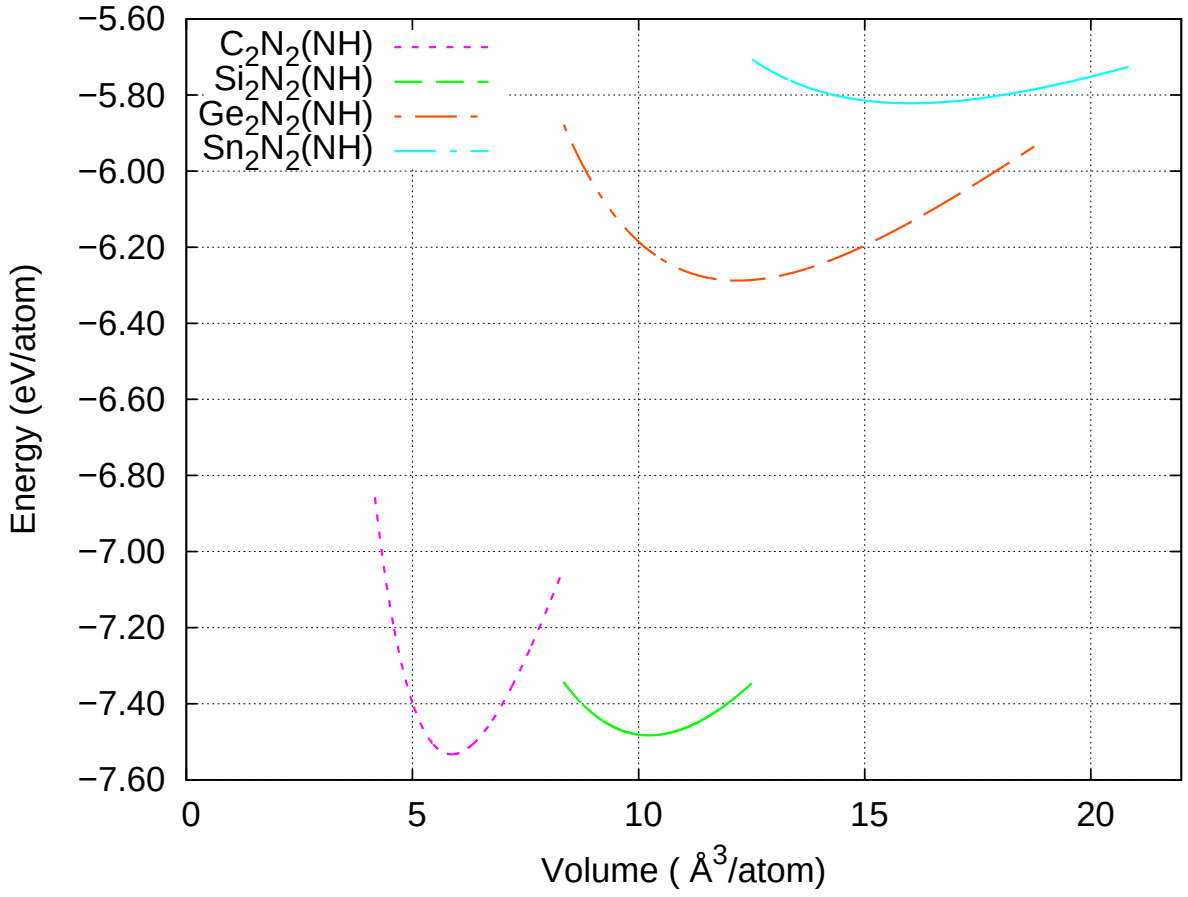


Figure 7.1 The curves showing energy per atom (eV) versus volume per atom(V) $Å^3$. The curves are obtained by fitting energy-volume data to third-order Birch-Murnaghan equations of states.

$Sn_2N_2(NH)$ and $Ge_2N_2(NH)$ offer minimal resistance to external pressure. The bulk modulus is an intrinsic property of the hardness of a material, thus a material with large bulk modulus should in nature be hard. Following this principle, both $Sn_2N_2(NH)$ and $Ge_2N_2(NH)$ are not hard materials. The nature and the size of chemical bonding in materials strongly contributes to the size of the bulk modulus. Shorter bond lengths yield large bulk modulus and vice versa. A systematic probe of bond lengths for compounds considered in this work show that the lengths ascend from C-N<Si-N<Ge-N<Sn-N. The strong covalent and hence shorter C-N bond lengths are responsible for the large bulk modulus in $C_2N_2(NH)$. Generally, from the sizes of M-N bonding (M=C,Si,Ge,Sn), it is apparent that $Ge_2N_2(NH)$ and $Sn_2N_2(NH)$ are softer than both $C_2N_2(NH)$ and $Si_2N_2(NH)$, because the bond lengths in Ge-N and Sn-N are longer than both in Si-N and C-N. The N-H bond lengths among the four compounds show hardly any variation within the precision

of our calculations, while H-H are weakly bonded. The calculated bond lengths are reported in Table 7.2. The theoretical predicted gravimetric densities(ρ) are listed in Table 7.1. The ρ for C_2N_2(NH), Si_2N_2(NH), Ge_2N_2(NH) and Sn_2N_2(NH) are 3.6gcm^{-3}, 3.0gcm^{-3}, 4.72gcm^{-3} and 5.13gcm^{-3} respectively. Both C_2N_2(NH) and Si_2N_2(NH) have a density closer to that of diamond (ρ=3.52gcm^{-3}), cubic boron nitride (ρ=3.45gcm^{-3}) and dense β-C_3N_4(ρ=3.57gcm^{-3}) [133]. Other nitrides like c-Si_3N_4 and β-Si_3N_4 have a density of ρ=3.93gcm^{-3} and ρ=3.21gcm^{-3} respectively [134].

Table 7.1 GGA-DFT calculated lattice constants (a, b and c) Å, gravimetric density (gcm^{-3}), volume per atom(V) Å^3, cohesive energy E_{coh}(eV), bulk modulus B_0 (GPa), and band gap E_g(eV). A comparison between experimental and other theoretical studies is also shown.

Compound	a (Å)	b (Å)	c (Å)	ρ(gcm^{-3})	V (Å^3)	E_{coh} (eV)	B_0 (GPa)	E_g(eV)
C_2N_2(NH)	7.676	4.493	4.037	3.6	5.87	-7.53	262	4.40
Others(LDA)[a]	7.572	4.442	4.003	(3.21±0.3)				
Others(GGA)[c]	7.682	4.518	4.054				256	4.36
Others(LDA)[c]	7.573	4.442	4.003				281	
Experiment[b]	7.618	4.483	4.038		5.74		258	
Si_2N_2(NH)	9.217	5.310	4.709	3.0	10.23	-7.48	107	5.22
Others(GGA)[c]	9.272	5.464	4.855					5.01
Others(LDA)[c]	9.137	5.343	4.785					
Experiment[d]	9.193	5.409	4.819					
Ge_2N_2(NH)	9.898	5.691	5.017	4.72	12.19	-6.28	62	2.66
Sn_2N_2(NH)	10.947	6.251	5.487	5.13	16.01	-5.82	32	1.05

[a]Ref. [47], [b]Ref. [48], [c]Ref. [49] [d]Ref. [51]

7.2 Density of states and band gap

In semiconducting materials, band gaps are classified as either being direct or indirect. The differences arise from the positions of the valence band maximum and the conduction band

minimum in the Brillouin zone. For instance, this work predicts $Si_2N_2(NH)$ and $Ge_2N_2(NH)$ to have a direct band gap of 5.22eV and 2.66eV respectively. This implies that both valence and conduction bands occur at the same *k*-vector in the Brillouin zone. However, for indirect band gaps materials such as $C_2N_2(NH)$ and $Sn_2N_2(NH)$ with calculated values as 4.40eV and 1.05eV respectively, the conduction band minimum occurs at different position in the Brillouin zone from that of valence band maximum. The computed band gaps for $C_2N_2(NH)$ and $Si_2N_2(NH)$ are in agreement with previous calculations listed in Table 7.1. Note, the nature of the band gap (direct or indirect) of a material significantly affects the recombination process in which electrons pair up with holes. The relevance of the nature of band gap features prominently in the study of optical properties of materials.

Table 7.2 GGA-DFT calculated bondlengths in Å units.

$C_2N_2(NH)$	C-C	C-N	C-H	N-H	N-N	H-H
	2.478	1.452	2.066	1.033	2.355	2.236
$Si_2N_2(NH)$	Si-Si	Si-N	Si-H	N-H	N-N	H-H
	2.910	1.719	2.323	1.028	2.727	2.538
$Ge_2N_2(NH)$	Ge-Ge	Ge-N	Ge-H	N-H	N-N	H-H
	3.114	1.857	2.431	1.029	2.932	2.817
$Sn_2N_2(NH)$	Sn-Sn	Sn-N	Sn-H	N-H	N-N	H-H
	3.417	2.054	2.590	1.030	3.216	3.175

7.3 Mechanical stability test

The mechanical stability tests reveals that $Si_2N_2(NH)$, $Ge_2N_2(NH)$ and $Sn_2N_2(NH)$ are stable structures. The stability test were carried out by calculating elastic constant c_{ij} following procedures stated in VASP. A comparison of computed elastic constants for $C_2N_2(NH)$, $Si_2N_2(NH)$, $Ge_2N_2(NH)$ and $Sn_2N_2(NH)$ are listed in Table 7.3. Good agreement between calculated elastic constants in this work and those reported in reference [49] were observed. The type of exchange correlation used generally affects the calculated elastic constants. LDA predicts slightly higher

Table 7.3 Calculated independent elastic constants in GPa units obtained using GGA.

Compound	Exchange-correlation	c_{11}	c_{12}	c_{13}	c_{22}	c_{23}	c_{33}	c_{44}	c_{55}	c_{66}
$C_2N_2(NH)$	GGA	594	79	94	554	73	810	321	207	210
	GGA[c]	597	89	107	567	79	804	335	221	222
	LDA[c]	616	80	103	576	71	871	347	221	218
$Si_2N_2(NH)$	GGA	271	29	42	195	23	298	136	78	57
	GGA[c]	285	38	43	195	26	313	125	62	75
	LDA[c]	302	83	79	255	47	375	147	86	109
$Ge_2N_2(NH)$	GGA	178	35	37	131	12	182	93	48	34
$Sn_2N_2(NH)$	GGA	124	27	25	85	3	86	61	31	26

[c]Ref. [49]

elastic constants as compared to GGA, because GGA overestimates lattice parameters, while LDA will normally underestimate lattice parameters.

7.4 Derived elastic properties

It is of great significance to accurately compute the elastic constant in order to derive quantities such as Vicker's hardness, inverse of Poisson's ratio, Young's, shear and bulk moduli of materials. In this case the derived quantities are listed in Table 7.4 and compared to available data from literature.

As has been indicted in previous chapters, hardness is a complex property of material that correlates with quantities listed in Table 7.4. The highly covalent $C_2N_2(NH)$ has Vickers hardness of about 50% less than that of diamond. Interestingly, the $C_2N_2(NH)$ has same magnitude of Vicker's hardness as that of cubic C_3N_4.

Table 7.4 First principles results for elastic bulk modulus B(GPa), shear modulus G(GPa), G/B, Young's modulus E(GPa), Poisson's ratio ν and predicted Vickers hardness H_v

Compound	Exchange-correlation	B	G	E	G/B	ν	H_v
$C_2N_2(NH)$	GGA	272	262	584	0.96	0.138	46
	GGA[a]	280	269	600	0.96	0.137	47
	LDA[a]	286	275	616	0.96	0.135	48
$Si_2N_2(NH)$	GGA	106	99	217	0.93	0.152	24
	GGA[a]	112	98	220	0.86	0.166	22
	LDA[a]	150	117	272	0.78	0.192	21
$Ge_2N_2(NH)$	GGA	73	62	138	0.85	0.180	15
$Sn_2N_2(NH)$	GGA	45	40	88	0.88	0.162	12

[a]Ref. [49]

7.5 Optical properties

FIG.7.2 show the imaginary (ε_2) and the real (ε_1) parts of dielectric function (ε) from 0-12eV for $C_2N_2(NH)$, $Si_2N_2(NH)$, $Ge_2N_2(NH)$ and $Sn_2N_2(NH)$. The imaginary part of the dielectric function also represents the optical absorption spectrum. The calculation was carried out within the random-phase approximation without the local field effects. Overall, the four isostructural compounds show some common features. For instance, the two main peaks in the ε_2 of $Sn_2N_2(NH)$ appears around 4eV and 6.4eV while in $Ge_2N_2(NH)$ they occurs at about 5.1eV and 7.7eV. For $C_2N_2(NH)$ and $Si_2N_2(NH)$ the prominent peaks occur at slightly higher energies of about 7.8eV and 12eV, and 7.2eV and 9.4eV respectively. In depth analysis of the ε_2, show that $Sn_2N_2(NH)$ has an exceptionally smaller absorption threshold when compared to $C_2N_2(NH)$, $Si_2N_2(NH)$ and $Ge_2N_2(NH)$. Normally, ε_1 is obtained from ε_2 via the Kramers-Kronig transformations [135]. The main peak in ε_1 of $Sn_2N_2(NH)$ is quite prominent, since it rises at 1.6 eV while similar peaks in the other compounds occur between 5-6eV.

Classifying the dielectric behaviour into infrared(IR), visible (V) and ultraviolet(UV) regimes, the following observations are made: First, within the IR regime, ε_1 and ε_2 of the four compounds look rather similar, except noticeable shift in ε_2 of $Sn_2N_2(NH)$ at the edges of the IR regime.

Table 7.5 GGA-DFT calculated dielectric constant along crystallographic axes $\mathbf{a}$, $\mathbf{b}$ and $\mathbf{c}$.

Compound	ε_a	ε_b	ε_c	ε_0
$C_2N_2(NH)$	4.75	5.04	4.72	4.84
$Si_2N_2(NH)$	3.90	4.03	4.05	3.99
$Ge_2N_2(NH)$	4.87	4.99	4.72	4.86
$Sn_2N_2(NH)$	5.00	5.19	4.61	4.93

Ideally, absorption would increase with decreasing wavelengths especially below wavelength corresponding to the band gap. Secondly, $Sn_2N_2(NH)$ starts absorbing within the the IR regime. The absorption strength is even higher for $Sn_2N_2(NH)$ within the visible range. Thirdly, the onset of absorption for $Ge_2N_2(NH)$ is within the visible range, though strong absorption occurs within the the UV regime. Lastly both $C_2N_2(NH)$ and $Si_2N_2(NH)$ remain featureless within the infrared and visible regimes. This confirms that $C_2N_2(NH)$ and $Si_2N_2(NH)$ are insulators. Note that for orthorhombic structures, it is reasonable to calculate components of dielectric function parallel to the crystallographic axes a, b and c. For clarity the components of dielectric function are presented as ε_a, ε_b and ε_c. However, in normal laboratory experiments, it is tedious to grow a single crystal, and hence it is preferable to perform experiments on polycrystalline samples. In such a case, it is insufficient or inaccurate to calculate ε_0 parallel to a single crystallographic axis. It makes more sense to present ε_0 as the average of ε_a, ε_b and ε_c, and results are as listed in Table 7.5. An important point to note here is that for anisotropic crystalline structures the polarizability is also anisotropic and it depends on the compound under consideration. For instance, $Ge_2N_2(NH)$ is highly polarised along the c axis and hence has a high dielectric constant along ε_c). On the other hand, $Si_2N_2(NH)$ turns out to have lower dielectric constant along ε_c.

The calculated refractive index n from the relation $n{=}\sqrt{\varepsilon}$ show that there is small variation of about 0.01 to 0.02 among the four compounds. It emerges that in spite of $Sn_2N_2(NH)$ having a small band gap, absorption threshold and a small plasmon peak, it has nevertheless highest n of about 2.21 while $C_2N_2(NH)$, $Si_2N_2(NH)$ and $Ge_2N_2(NH)$ have an n of about 2.19, 2.00 and 2.20 respectively. We see that narrow/small band gap materials have high refractive index and high dielectric constant. This phenomenon is attributed to how electric fields interact with

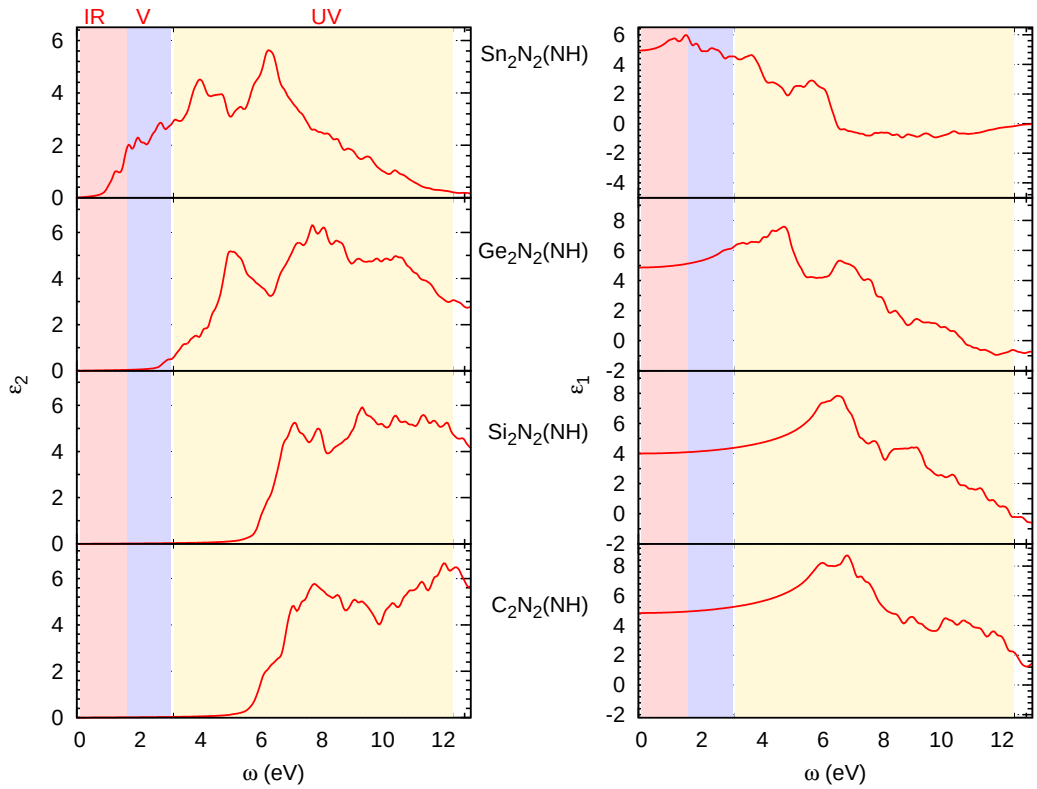


Figure 7.2 The averaged imaginary and real part of frequency depended dielectric function. The Infrared (IR), visible (V) and utraviolet (UV) spectral regions are indicated in the figure

electrons and how electrons freely moves in available electronic states found in valence and conduction bands. It is obvious that narrow band gaps allows electrons to drift easily within electronic states as opposed to large band gaps. Once the electric field interacts with electrons, the electronic charges get polarised and the level of polarisation is linearly correlated with the dielectric constants.

7.6 Summary

This work aimed at providing details of first principles investigation of the structural, electronic and optical properties of $C_2N_2(NH)$, $Si_2N_2(NH)$ and $Ge_2N_2(NH)$. The four compounds are isostructural though each one of them displays quite unique elastic and electronic properties. The newly predicted $Sn_2N_2(NH)$ and $Ge_2N_2(NH)$ are mechanically stable. The Vickers hardness has been

predicted by relating it to shear and bulk moduli. The inverse of the Poisson's ratio has been deduced as a relevant indicator of hardness. The low compressible $C_2N_2(NH)$ has a similar magnitude of Vickers hardness as the cubic-C_3N_4, but less than that of CN_2.

8. Conclusions and future studies

This chapter reviews the purpose of this research work, the methodology, the results obtained and close with remarks on future work.

8.1 Conclusions

The purpose of this research was to fill some gaps in our understanding of the properties of carbon-nitrogen materials, and to provide salient information on future applications of these materials. Several specific objectives were put forward to guide the investigations, and to many results were reported in peer reviewed journals. Density functional theory has been a useful and reliable tool throughout the current work. The following accomplishments have been made on the various compounds studied in this work.

8.1.1 C_3N_4. The present work has provided an overview of the elastic properties of the hypothetical superhard C_3N_4. The elastic constants and derived quantities such as bulk, shear and Young's moduli have been discussed for various candidates of stable crystalline structures. The seven phases of C_3N_4 studied in this work were divided into cubic and layered crystal structures. The hardness of the cubic polymorphs were emphasized, in order to mainly settle a long-standing controversy that exists in the literature about the hardness of cubic C_3N_4.

A comprehensive study of the relative phase stabilities, phase transformations, electronic and the frequency dependent optical properties of various polymorphs of C_3N_4 have been reported. The real and imaginary parts of the dielectric function provide useful information to work out the reflectivity, absorption, refractive index and electron energy loss spectrum. Optical properties of the C_3N_4 phases may become an important guide for the experimentalist who wants to synthesize and study these compounds. All the phases of C_3N_4 are semiconductors, some of them with wide band gaps that could make them interesting for applications in semiconductor technology.

8.1.2 dinitrides. As one of the key objectives of this thesis, a thorough investigation of the phase transformations of carbon dinitride CN_2 was conducted, and the following conclusions can

be drawn from the results obtained.

1. CN_2 exists in numerous stable phases in a pressure range of 0-100 GPa. The lattice constants, bulk modulus, pressure derivatives of these phases have been calculated and they are in good agreement with previous theoretical values. No experimental results were found in the literature.

2. Some of the stable phases showed degeneracies in their ground state energies. For instance cmc21-CN_2 and I42m-CN_2 are competing phases though I42m-CN_2 is very dense and the least compressible phase of CN_2.

3. The layered pc-CN_2 phase is energetically favourable at low pressure, while the cubic pa3-CN_2 is the high energy structure occurring at high pressure.

4. The energetically favourable pc-CN_2 phase will transform into several high pressure phases when pressure is induced. Such pressure induced phase transitions are always accompanied by volume reductions and an increment in density.

The silicon dinitride (SiN_2) and germinium dinitride (GeN_2) adopt similar crystal structure as CN_2. Analysis of the electronic, elastic and optical properties of CN_2, SiN_2 and GeN_2 were carried out and a comparison performed for different exchange correlation functionals. From the band structure calculations, SiN_2 and GeN_2 are found to be indirect band gap materials, while CN_2 has a wide direct band gap. Elastic properties reveals that CN_2 is a potential ultrahard material with shear modulus which is about 31% lower than that of diamond. The main features of the optical spectra of GeN_2 is within the solar spectrum as inferred from its small band gap, while for CN_2 and SiN_2, the main features are within the ultraviolet range. These results provide guidance for further explorations of ultrahard materials as well as their potential applications in optoelectronic devices.

8.1.3 Imide group. First principles studies were applied on the imide group consisting of $C_2N_2(NH)$, $Si_2N_2(NH)$ and $Ge_2N_2(NH)$. Several electronic structure properties were reported. To begin with, structural optimization were performed for each compound within a defective orthorhombic crystal structure, and the mechanical stability of these structures was ascertained.

The resulting equilibrium lattice parameters, bulk modulus, pressure derivative of bulk modulus and minimum total energies were reported. For $C_2N_2(NH)$ and $Si_2N_2(NH)$, the results obtained in the current work were in good agreement with other theoretical and experimental work. Furthermore, the elastic constants, band gaps and optical properties of $C_2N_2(NH)$, $Si_2N_2(NH)$ and $Ge_2N_2(NH)$ were also investigated. The resistance to change in volume and shape were predicted by computing the bulk and shear moduli respectively. The Vickers hardness was estimated and correlated with quantities such as the inverse of Poisson's ratio, shear and bulk moduli.

It emerges from the computed band gaps of $Si_2N_2(NH)$ and $Ge_2N_2(NH)$ that these are direct band gap materials whereas $C_2N_2(NH)$ and $Sn_2N_2(NH)$ are predicted to have an indirect band gap. $C_2N_2(NH)$ and $Si_2N_2(NH)$ may be regarded as large band gap materials or insulators, based on the fact that the used exchange correlation functionals are known to underestimate band gaps. $Ge_2N_2(NH)$ and $Sn_2N_2(NH)$ have relatively small band gaps, compared to both $C_2N_2(NH)$ and $Si_2N_2(NH)$.

8.2 Future work

Present work leaves a number of open questions to be filled in the future:

1. The optical properties studied answered on an independent particle picture level cannot be directly compared with experimental optical spectra. Better comparison is only achieved by inclusion of excitonic effects via the so called Bethe-Salpeter equation [132].

2. Better band gaps are obtained if one performs calculations with GW and hybrid functionals. These studies can be performed with future access to sufficient computational resources and computing time.

3. Thermodynamic stabilities, vibrational frequencies, heat capacity and wave velocities are significant properties that could be investigated as well, and which might lead to interesting applications of the materials studied in this thesis.

Appendix A. Conferences and workshops

Conferences

1. DST-NRF Student presentation(2014), University of Witwatersrand, Johannesburg .
2. The 7th International Conference of the Africa Materials Research Society, Addis Ababa, Ethiopia, December 8-13, 2013. Oral presentation on

   "**Aspects of computational properties of material**"
3. DST/NRF Student presentation(2012)., University of Witwatersrand, Johannesburg.
4. Condensed Matter and Materials Physics Division 2011 (CMMP11) 13 - 15 December 2011, Lancashire County Cricket Club, Manchester, UK. Conference organised by the IOP Condensed Matter and Materials Physics Division. Oral presentation on
5. DST-NRF Student presentation(2011), University of the Witwatersrand, Johannesburg. Poster presentation on

   "**Ab – initio study of various superhard and graphitic structures of**$\mathbf{C_3N_4}$"
6. CHPC National Meeting, Capetown, South Africa, December 2010.
7. Moi University 5th International Conference, Eldoret Kenya, August 2009.

Workshops

1. Yambo hands-on tutorial on electronic and optical excitations: from basic to advanced applications, April 8, 2013 to April 12, 2013 CECAM-HQ-EPFL, Lausanne, Switzerland, Role: Participant.
2. 6th International Workshop on Spinel Nitrides and Related Materials in Conjunction with the Marie Curie ITN 7th Framework Programme FUNEA 9th to 14th September, 2012 Ruedesheim/Rhine, Germany. Oral presentation on

"**Optical properties of diamond – like, layered and buckled phases C_3N_4**"

3. The African School series on Electronic Structure Methods and Applications (ASESMA), Eldoret Kenya, May-June 2012. Role: Tutor.

4. The African School series on Electronic Structure Methods and Applications (ASESMA), Capetown, South Africa, July 2010. Role: Participant.

Appendix B. Curriculum vitae

George Simiyu Manyali

Personal information

Nationality	Kenyan
Sex	Male
Date of birth	24/09/1981
Wife	Pamela Nafula
Son	Nicola Chetty
Parents	Topisita Manyali and Erick Manyali
email	georgemanyali@gmail.com

Education

2012-2014	Doctoral studies in Physics at the University of the Witwatersrand, Johannesburg. PhD thesis: "A computational study of layered and superhard carbon-nitrogen material"
June 2012	Graduated with Distinction and awarded academic degree of Master of Science.
2011	Master of Science studies in Physics at the University of the Witwatersrand, Johannesburg. Dissertation: "Ab-initio study of elastic and structural properties of layered nitride materials"
December, 2008	Graduated with Second class honours, upper division and awarded academic degree of Bachelor of Science with honours.
2004-2008:	Studies in Physics and mathematics at Moi University, Eldoret Kenya.
1998-2002:	Secondary education at Sinoko Secondary School, Kitale Kenya (K.C.S.E grade B+)
1989-1997:	Primary education, Sinoko Primary School, Kitale Kenya (K.C.P.E 455/700 marks).

References

[1] R. Warmbier, G. S. Manyali, A. Quandt, Phys. Rev. B 85 (2012) 085442.

[2] G. S. Manyali, R. Warmbier, A. Quandt, J. E. Lowther, Comput. Mater. Sci. 69 (2013) 299–303.

[3] G. S. Manyali, R. Warmbier, A. Quandt, Comput. Mater. Sci. 79 (2013) 710–714.

[4] A. Quandt, R. Warmbier, G. Manyali, in: Electromagnetics in Advanced Applications (ICEAA), 2012 International Conference on, IEEE, 2012, pp. 408–411.

[5] R. Warmbier, A. Quandt, G. Manyali, in: Electromagnetics in Advanced Applications (ICEAA), 2012 International Conference on, IEEE, 2012, pp. 470–473.

[6] A. Quandt, R. Warmbier, G. S. Manyali, in: Transparent Optical Networks (ICTON), 2012 14th International Conference on, IEEE, 2012, pp. 1–4.

[7] G. S. Manyali, R. Warmbier, A. Quandt, Comput. Mater. Sci. (0) (2014) –.

[8] L. Zhang, R. Erni, J. Verbeeck, G. Van Tendeloo, Phys. Rev. B 77 (2008) 195119.

[9] G. S. Manyali, Ab-initio study of elastic and structural properties of layered nitride materials, Master's thesis, University of the Witwatersrand, Johannesburg (2012).

[10] X.-Q. Chen, H. Niu, D. Li, Y. Li, Intermetallics 19 (9) (2011) 1275–1281.

[11] A. Liu, R. Wentzcovitch, Phys. Rev. B 50 (14) (1994) 10362.

[12] A. C. Neto, F. Guinea, N. Peres, K. S. Novoselov, A. K. Geim, Rev. Mod. Phys. 81 (1) (2009) 109.

[13] D. Chung, J. Mater. Sci. 37 (8) (2002) 1475–1489.

[14] K. S. Novoselov, A. K. Geim, S. Morozov, D. Jiang, Y. Zhang, S. Dubonos, I. Grigorieva, A. Firsov, Science 306 (5696) (2004) 666–669.

[15] M. Gullans, D. Chang, F. Koppens, F. G. de Abajo, M. Lukin, Phys. Rev. Lett. 111 (24) (2013) 247401.

[16] M. J. Allen, V. C. Tung, R. B. Kaner, Chem. Rev. 110 (1) (2009) 132–145.

[17] A. Liu, M. Cohen, Science 245 (4920) (1989) 841.

[18] D. Teter, R. Hemley, Science 271 (5245) (1996) 53–55.

[19] Y. Gogotsi, V. Domnich, High pressure surface science and engineering, CRC Press, 2003.

[20] A. Zerr, G. Miehe, G. Serghiou, M. Schwarz, E. Kroke, R. Riedel, H. Fueß, P. Kroll, R. Boehler, Nature 400 (6742) (1999) 340–342.

[21] J. Lowther, Physica B 358 (1) (2005) 72–76.

[22] F. Gao, R. Xu, K. Liu, Phys. Rev. B 71 (5) (2005) 052103.

[23] P. Hohenberg, W. Kohn, Phys. Rev. 136 (3B) (1964) B864–B871.

[24] W. Kohn, L. J. Sham, Phys. Rev. 140 (4A) (1965) A1133–A1138.

[25] G. Bergerhoff, I. Brown, Crystallographic databases, (IUCr) (1987) 77–95.

[26] A. Belsky, M. Hellenbrandt, V. L. Karen, P. Luksch, Acta Cryst. B 58 (3) (2002) 364–369.

[27] A. Jain, S. P. Ong, G. Hautier, W. Chen, W. D. Richards, S. Dacek, S. Cholia, D. Gunter, D. Skinner, G. Ceder, K. A. Persson, Appl. Phys. Lett. Mat. 1 (1) (2013) 011002.

[28] S. Curtarolo, W. Setyawan, S. Wang, J. Xue, K. Yang, R. H. Taylor, L. J. Nelson, G. L. Hart, S. Sanvito, M. Buongiorno-Nardelli, et al., Comput. Mater. Sci. 58 (2012) 227–235.

[29] J. N. Hart, F. Claeyssens, N. L. Allan, P. W. May, Phys. Rev. B 80 (17) (2009) 174111.

[30] J. Lowther, Phys. Rev. B 57 (10) (1998) 5724–5727.

[31] A. Reyes-Serrato, D. Galván, I. Garzón, Phys. Rev. B 52 (9) (1995) 6293.

[32] F. Ding, Y. Feng, Comput. Mater. Sci. 30 (3) (2004) 364–370.

[33] G. Rignanese, J. Charlier, X. Gonze, Phys. Rev. B 66 (20) (2002) 205416.

[34] S.-D. Mo, L. Ouyang, W. Ching, I. Tanaka, Y. Koyama, R. Riedel, Phys. Rev. Lett. 83 (24) (1999) 5046–5049.

[35] P. Zinin, L.-C. Ming, S. Sharma, V. Khabashesku, X. Liu, S. Hong, S. Endo, T. Acosta, Chem. Phys. Lett. 472 (1-3) (2009) 69–73.

[36] L. Ming, P. Zinin, Y. Meng, X. Liu, S. Hong, Y. Xie, J. Appl. Phys. 99 (3) (2006) 033520.

[37] I. Alves, G. Demazeau, W. F. Tanguy, B., Solid State Commun. 109 (11) (1999) 697–701.

[38] H. Zhao, X. Chen, C. Jia, T. Zhou, X. Qu, J. Jian, Y. Xu, T. Zhou, Mater. Sci. and Eng. B-Adv. 122 (3) (2005) 226–230.

[39] D. Shi, X. Zhang, L. Yuan, Y. Gu, Y. Zhang, Z. Duan, X. Chang, Z. Tian, N. Chen, Appl. Surf. Sci. 148 (1-2) (1999) 50–55.

[40] J. He, L. Guo, X. Guo, R. Liu, Y. Tian, H. Wang, C. Gao, Appl. Phys. Lett. 88 (10) (2006) 101906–101906.

[41] X. Wang, K. Maeda, A. Thomas, K. Takanabe, G. Xin, J. M. Carlsson, K. Domen, M. Antonietti, Nat. Mater. 8 (1) (2008) 76–80.

[42] R. Musin, D. Musaev, M. Lin, J. Phys. Chem. B 103 (5) (1999) 797–803.

[43] R. Weihrich, S. F. Matar, E. Betranhandy, V. Eyert, Solid State Sci. 5 (5) (2003) 701–703.

[44] R. Weihrich, V. Eyert, S. F. Matar, Chem. Phys. Lett. 373 (5) (2003) 636–641.

[45] Q. Li, H. Liu, D. Zhou, W. Zheng, Z. Wu, Y. Ma, Phys. Chem. Chem. Phys 14 (37) (2012) 13081–13087.

[46] S. Cahangirov, M. Topsakal, E. Aktürk, H. Şahin, S. Ciraci, Phys. Rev. Lett. 102 (2009) 236804.

[47] E. Horvath-Bordon, R. Riedel, P. F. McMillan, P. Kroll, G. Miehe, P. A. van Aken, A. Zerr, P. Hoppe, O. Shebanova, I. McLaren, et al., Angew. Chem. Int. Edit. 46 (9) (2007) 1476–1480.

[48] A. Salamat, K. Woodhead, P. McMillan, R. Cabrera, A. Rahman, D. Adriaens, F. Corà, J. Perrillat, Phys. Rev. B 80 (2009) 104106.

[49] H. Yan, Q. Wei, B. Zheng, P. Guo, J. Solid State Chem. 184 (2011) 572–577.

[50] K. Takarabe, M. Sougawa, H. Kariyazaki, K. Sueoka, J. Appl. Phys. 112 (2012) 013537–013537.

[51] H. J. J. D. Peters, Less-Common Met. 146 (1989) 241.

[52] Y. Ding, M. Chen, W. Wu, Physica B 428 (2013) 97–105.

[53] M. Sougawa, K. Takarabe, Y. Mori, T. Okada, T. Yagi, H. Kariyazaki, K. Sueoka, J. Appl. Phys. 113 (5) (2013) 053510.

[54] C. Fiolhais, F. Nogueira, M. A. Marques, A primer in density functional theory, Vol. 620, Springer, 2003.

[55] R. M. Martin, Electronic structure: basic theory and practical methods, Cambridge University Press, 2004.

[56] W. Kohn, A. Becke, R. Parr, J. Phys. Chem. 100 (31) (1996) 12974–12980.

[57] G. Kresse, J. Hafner, Phys. Rev. B 47 (1) (1993) 558.

[58] G. Kresse, J. Hafner, Phys. Rev. B 49 (20) (1994) 14251.

[59] D. Hobbs, G. Kresse, J. Hafner, Phys. Rev. B 62 (17) (2000) 11556.

[60] G. Kresse, J. Furthmuller, Comput. Mater. Sci. 6 (1) (1996) 15–50.

[61] M. Levy, P Natl. Acad. Sci. USA 76 (12) (1979) 6062.

[62] J. P. Perdew, A. Zunger, Phys. Rev. B 23 (10) (1981) 5048–5079.

[63] T. C. Leung, C. T. Chan, B. N. Harmon, Phys. Rev. B 44 (7) (1991) 2923.

[64] C. S. Wang, B. M. Klein, H. Krakauer, Phys. Rev. Lett 54 (16) (1985) 1852–1855.

[65] M. Grüning, A. Marini, A. Rubio, J. Chem. Phys. 124 (2006) 154108.

[66] S. Lebègue, M. Klintenberg, O. Eriksson, M. Katsnelson, Phys. Rev. B 79 (24) (2009) 245117.

[67] P. Rinke, A. Qteish, J. Neugebauer, C. Freysoldt, M. Scheffler, New J. Phys. 7 (2005) 126.

[68] J. P. Perdew, J. Chevary, S. Vosko, K. Jackson, M. Pederson, D. Singh, C. Fiolhais, Phys. Rev. B 46 (11) (1992) 6671.

[69] J. P. Perdew, K. Burke, M. Ernzerhof, Phys. Rev. Lett 77 (18) (1996) 3865–3868.

[70] J. P. Perdew, K. Burke, M. Ernzerhof, Phys. Rev. Lett 80 (4) (1998) 891–891.

[71] A. El-Barbary, First principles characterisation of defects in irradiated graphitic materials, Ph.D. thesis, University of Sussex (2005).

[72] D. J. Singh, L. Nordström, Planewaves, Pseudopotentials, and the LAPW method, Springer Verlag, 2006.

[73] V. Ozoliņš, M. Körling, Phys. Rev. B 48 (1993) 18304–18307.

[74] E. I. Proynov, E. Ruiz, A. Vela, D. Salahub, Int. J Quantum Chem. 56 (S29) (1995) 61–78.

[75] J. Tao, J. P. Perdew, V. N. Staroverov, G. E. Scuseria, Phys. Rev. B 91 (14) (2003) 146401.

[76] J. Heyd, J. E. Peralta, G. E. Scuseria, R. L. Martin, J. Chem. Phys. 123 (2005) 174101.

[77] J. Paier, M. Marsman, K. Hummer, G. Kresse, I. C. Gerber, J. G. Ángyán, J. chem. Phys. 124 (2006) 154709.

[78] L. Hedin, Phys. Rev. 139 (3A) (1965) A796.

[79] F. Tran, P. Blaha, Phys. Rev. lett. 102 (22) (2009) 226401.

[80] A. D. Becke, E. R. Johnson, J. Chem. Phys 124 (22) (2006) 221101.

[81] N. W. Ashcroft, N. D. Mermin, Solid state phys., Saunders, Philadelphia, 1976.

[82] M. C. Payne, M. P. Teter, D. C. Allan, T. Arias, J. Joannopoulos, Rev. Mod. Phys. 64 (4) (1992) 1045–1097.

[83] H. Monkhorst, J. Pack, Phys. Rev. B 13 (12) (1976) 5188–5192.

[84] D. Chadi, M. L. Cohen, Phys. Rev. B 8 (12) (1973) 5747.

[85] M. Cohen, V. Heine, Solid State Phys. 24 (1970) 37–248.

[86] J. Phillips, L. Kleinman, Phys. Rev. 116 (2) (1959) 287.

[87] G. B. Bachelet, D. R. Hamann, M. Schluter, Phys. Rev. B 26 (8) (1982) 4199.

[88] N. Troullier, J. L. Martins, Phys. Rev. B 43 (3) (1991) 1993.

[89] A. Rappe, K. Rabe, E. Kaxiras, J. Joannopoulos, Phys. Rev. B 41 (2) (1990) 1227.

[90] L. Kleinman, D. Bylander, Phys. Rev. Lett 48 (20) (1982) 1425–1428.

[91] J. Hutter, H. Luthi, M. Parrinello, Comput. Mater. Sci. 2 (2) (1994) 244–248.

[92] D. Vanderbilt, Phys. Rev. B 41 (11) (1990) 7892.

[93] G. Kresse, D. Joubert, Phys. Rev. B 59 (3) (1999) 1758–1775.

[94] D. Hamann, M. Schluter, C. Chiang, Phys. Rev. Lett 43 (20) (1979) 1494–1497.

[95] N. Holzwarth, G. Matthews, R. Dunning, A. Tackett, Y. Zeng, Phys. Rev. B 55 (4) (1997) 2005.

[96] P. E. Blöchl, Phys. Rev. B 50 (24) (1994) 17953.

[97] D. C. Langreth, M. Dion, H. Rydberg, E. Schröder, P. Hyldgaard, B. I. Lundqvist, Int. J. Quantum chem. 101 (5) (2005) 599–610.

[98] S. Grimme, J. Comput. Chem 25 (12) (2004) 1463–1473.

[99] H. Rydberg, M. Dion, N. Jacobson, E. Schröder, P. Hyldgaard, S. Simak, D. C. Langreth, B. I. Lundqvist, Phys. Rev. Lett. 91 (12) (2003) 126402.

[100] M. Dion, H. Rydberg, E. Schröder, D. C. Langreth, B. I. Lundqvist, Phys. Rev. Lett. 92 (24) (2004) 246401.

[101] S. Grimme, J. Comput. Chem 27 (15) (2006) 1787–1799.

[102] M. Gajdoš, K. Hummer, G. Kresse, J. Furthmüller, F. Bechstedt, Phys. Rev. B 73 (2006) 045112.

[103] W. A. Harrison, Elementary electronic structure, World Scientific, 1999.

[104] A. M. Fox, Optical properties of solids, Vol. 3, Oxford University Press, 2001.

[105] N. Wiser, Phys. Rev. 129 (1963) 62–69.

[106] D. M. Ceperley, B. Alder, Phys. Rev. Lett 45 (7) (1980) 566–569.

[107] Y. Xu, S.-P. Gao, Int. J. Hydrogen Energy 37 (15) (2012) 11072–11080.

[108] F. Birch, Phys. Rev. 71 (11) (1947) 809.

[109] M. S. H. Suleiman, A theoretical investigation of structural, electronic and optical properties of some group 10, 11 and 12 transition-metal nitrides, Ph.D. thesis, University of the Witwatersrand (2013).

[110] N. Mounet, N. Marzari, Phys. Rev. B 71 (20) (2005) 205214.

[111] M. H. Grimsditch, A. K. Ramdas, Phys. Rev. B 11 (1975) 3139–3148.

[112] P. Y. Yu, M. Cardona, Fundamentals of semiconductors: physics and materials properties, Springer Berlin, 1999.

[113] X. Gonze, C. Lee, Phys. Rev. B 55 (1997) 10355–10368.

[114] X. Wu, D. Vanderbilt, D. R. Hamann, Phys. Rev. B 72 (2005) 035105.

[115] J. Hu, W. Cheng, S. Huang, D. Wu, Z. Xie, Appl. Phys. Lett. 89 (26) (2006) 261117–261117.

[116] N. Wada, P. Gaczi, S. Solin, J. Non-Cryst. Solids 35 (1980) 543–548.

[117] A. Marinopoulos, L. Reining, V. Olevano, A. Rubio, T. Pichler, X. Liu, M. Knupfer, J. Fink, Phys. Rev. Lett. 89 (7) (2002) 076402.

[118] A. J. Cohen, P. Mori-Sánchez, W. Yang, Phys. Rev. B 77 (11) (2008) 115123.

[119] L. Sham, M. Schlüter, Phys. Rev. Lett 51 (20) (1983) 1888.

[120] F. Bruneval, N. Vast, L. Reining, Phys. Rev. B 74 (4) (2006) 045102.

[121] S. Raju, E. Mohandas, V. Raghunathan, J. Phys. Chem. Solids 58 (9) (1997) 1367–1373.

[122] C. L. Baker, F. J. Lincoln, A. W. S. Johnson, Acta Crystall. B-Stru 47 (6) (1991) 891–899.

[123] J. Lowther, Phys. Rev. B 62 (1) (2000) 5.

[124] W. Ching, S.-D. Mo, I. Tanaka, M. Yoshiya, Phys. Rev. B 63 (6) (2001) 064102.

[125] M. P. Shemkunas, G. H. Wolf, K. Leinenweber, W. T. Petuskey, J. Am. Ceram. Soc. 85 (1) (2002) 101–104.

[126] G. Serghiou, G. Miehe, O. Tschauner, A. Zerr, R. Boehler, J. Chem. Phys. 111 (1999) 4659–4662.

[127] W. Voigt, Lehrbuch der Kristallphysik:(mit Ausschluss der Kristalloptik), Vol. 34, BG Teubner, 1928.

[128] M. Born, K. Huang, Dynamical theory of crystal lattices, Oxford University Press, 1954.

[129] P. Ravindran, L. Fast, P. Korzhavyi, B. Johansson, J. Wills, O. Eriksson, J. Appl. Phys.. 84 (1998) 4891.

[130] S. Pugh, Philos. Mag. Series 7 45 (367) (1954) 823–843.

[131] H. Dixit, R. Saniz, S. Cottenier, D. Lamoen, B. Partoens, J. Phys.: Condens. Matter 24 (20) (2012) 205503.

[132] E. E. Salpeter, H. A. Bethe, Phys. Rev. 84 (1951) 1232–1242.

[133] J. Hu, P. Yang, C. M. Lieber, Phys. Rev. B 57 (6) (1998) R3185.

[134] R. Riedel, I.-W. Chen, Ceramics Science and Technology, Materials and Properties, Vol. 2, John Wiley & Sons, 2011.

[135] R. Kronig, J. Opt. Soc. Amer. 12 (6) (1926) 547–556.